



GRIT: A Package for Structure-Preserving Simulations of Gravitationally Interacting Rigid Bodies

Renyi Chen¹, Gongjie Li², and Molei Tao¹

¹ School of Mathematics, Georgia Institute of Technology, Atlanta, GA 30332, USA

² Center for Relativistic Astrophysics, School of Physics, Georgia Institute of Technology, Atlanta, GA 30332, USA; gongjie.li@physics.gatech.edu

Received 2021 March 23; revised 2021 June 6; accepted 2021 June 23; published 2021 September 22

Abstract

The spin-orbit coupling of planetary systems plays an important role in the dynamics and habitability of planets. However, symplectic integrators that can accurately simulate not only how orbit affects spin but also how spin affects orbit have not been constructed for general systems. Thus, we develop symplectic Lie-group integrators to simulate systems consisting gravitationally interacting rigid bodies. A user friendly package (GRIT³) is provided and external forcings, such as tidal interactions, are also included. As a demonstration, this package is applied to Trappist-I. The results show that the differences in transit-timing variations due to spin-orbit coupling could reach a few min in 10-year measurements, and strong planetary perturbations can push Trappist-I f, g and h out of the synchronized states.

Unified Astronomy Thesaurus concepts: Exoplanet dynamics (490); Planetary dynamics (2173); Celestial mechanics (211); Few-body systems (531); Black hole spin-flip (160); Oblateness (1143)

1. Introduction

Among thousands of detected exoplanetary systems, a significant fraction of them involve planets with close-in orbits. In particular, the occurrence rate for compact systems (e.g., multiple planets with periods of less than 10 days) is estimated to be $\sim 20\%-30\%$ (Muirhead et al. 2015; Zhu et al. 2018). The close separations between the planets allow strong planetary interactions that could lead to rich features in the dynamical evolution of the compact planetary systems.

Spin-axis dynamics are very interesting in compact planetary systems. For instance, rotational and tidal distortion of the planets can lead to orbital precession due to planet spin-orbit coupling, and this causes variations in transit timing. Recently, Bolmont et al. (2020) showed that the transit-timing variations (TTVs) due to spin-orbit coupling could be detectable for Trappist-I, which could in turn help us to constrain the physical properties of the planets. In addition, although tidal effects are strong for planets with close-in orbits, strong interactions between the planets could push these planets (with orbital periods in ~ 10 days) out of synchronized states (Vinson et al. 2019). Moreover, secular resonance-driven spin-orbit coupling could drive to large obliquity variations and lead to obliquity tides (Li 2021). This sculpts the exoplanetary systems: the obliquity tide could explain the overabundance of planet pairs that reside just wide of the first order mean-motion resonances (Millholland & Laughlin 2019).

Integrators involving spin-axis coupling have been developed to study these effects. There are mainly two different approaches: 1) evolving the orbital dynamics separately from the spin-axis evolutions (e.g., Laskar & Robutel 1993; Li & Batygin 2014; Vinson et al. 2019); and 2) evolving the spin and orbit evolution simultaneously (e.g., Hut 1981; Eggleton et al. 1998; Mardling & Lin 2002; Lissauer et al. 2012; Bolmont et al. 2015; Blanco-Cuaresma & Bolmont 2017; Millholland & Laughlin 2019). In the first approach, the orbital evolution of the system is first integrated using N -body simulation packages

assuming the objects are point-mass particles, and then spin-axis dynamics are computed using the results of the orbital evolution. This approach assumes that the effects of the spin on orbital dynamics are weak. In the second approach, additional force due to spin-orbit coupling is included in the N -body simulation package, which could affect both the orbital and spin-axis evolution.

To carefully study the effects of spin-orbit coupling, we develop a symplectic algorithm (“Gravitationally interacting Rigid-body InTegrator”, GRIT) starting with the first-principal rigid-body dynamics, so that the mutual interactions between spin and orbital dynamics can be accurately accounted for. A symplectic Lie-Poisson integrator for a rigid body has already been constructed in the seminal work of Touma & Wisdom (1994) for systems with near-Keplerian orbits, focusing on a system with one rigid body (for systems with more than one rigid body, the spin dynamics of each rigid body is considered separately under its own frame). However, for systems that involve close encounters, the orbits of objects are no longer Keplerian. In addition, the original version of the method in Touma & Wisdom (1994) was not high-order (in the time step). Building upon the existing progress, we no longer assume near-Keplerian orbits for wider applicability, and our package includes several high-order implementations. Moreover, we put all the bodies under the same inertia frame, such that the spin-orbit interactions are all considered altogether in one Hamiltonian framework. We also note that symplectic integrators for secular spin-orbit dynamics have been developed by Breiter et al. (2005), while our method is based on direct (non-secular) numerical simulations and therefore suitable for resonant situations.

The development of our integrator is tightly based on the profound field of geometric integration because rigid-body dynamics can be intrinsically characterized by mechanical systems on Lie groups. More precisely, the phase space is $T^*\mathbf{SE}(3)^{\otimes n}$, where n is the number of interacting bodies and the special Euclidean group $\mathbf{SE}(3)$ is where the center of mass and rotational orientation of each body lives. How to properly simulate such systems in a structure-preserving way, so that

³ <https://github.com/GRIT-RBSim/GRIT>

symplecticity can be conserved and the dynamics remain on the Lie group, has been extensively studied—for example, see Iserles et al. (2000), Bou-Rabee & Marsden (2009), Celledoni et al. (2014) for general Lie-group integrators, and (more broadly) Hairer et al. (2006), Leimkuhler & Reich (2004), Blanes & Casas (2017), Sanz-Serna & Calvo (1994) for monographs on geometric integration.

Regarding rigid-body integrators in particular, the following is an incomplete list in addition to Touma & Wisdom (1994). First, the work of Dullweber et al. (1997) used a splitting approach—similar to Touma & Wisdom (1994) in essence, but split differently—to construct symplectic and Lie-group-preserving integrators for rigid molecules. The main idea is to split the Hamiltonian into a free rigid-body part, including both translational and rotational kinetic energies, plus a potential part. The latter can be exactly integrated, and the former can also be exactly integrated when the rigid body is axial symmetric; otherwise, it is further split into a symmetric top and a correction term, both of which can be exactly integrated in a cheap way (without using special functions). The methods in the proposed package (which are explicit, high-order integrators) are largely based on this idea. Second, we note various splitting schemes for integrating free rigid bodies were compared in Fassò (2003). Recall that the free rigid body is integrable, and its numerical simulation based on multiple ways of expressing the exact solution were also proposed (e.g., van Zon & Schofield 2007; Celledoni et al. 2008), but the exact expressions involve special functions (unless the bodies are axial symmetric), which can be computationally expensive. Moreover, the “exact” solutions are not exact due to round-off errors, and this complication is studied (and remedied) in Vilmart (2008). For simple and robust arithmetic, the free rigid-body part of our method will be based on a sub-splitting into an axial-symmetric part and a small correction because most rotating celestial bodies relevant to this study are (almost) axial-symmetric. It is also worth mentioning that geometric integrators for (non-free but) gravitationally interacting rigid bodies have also been proposed. Touma & Wisdom (1994) and Lee et al. (2007) also constructed variational integrators using elegant geometric treatments. However, these integrators are implicit and computational efficiency is hence not optimal.

Given that we are interested in gravitationally interacting rigid bodies, GRIT uses tailored splitting schemes. Therefore, the existence of small parameters and separation of timescales in the system is utilized so that a better trade-off between efficiency and accuracy can be achieved (see Section 3.3.2 for details). Our treatment is, of course, based on extensive existing studies of splitting methods. Some more general discussions on splitting methods can be found, for example, in McLachlan & Quispel (2002), Blanes et al. (2008), and Blanes et al. (2013).

This article is organized as follows. Section 2 describes the rigid-body formulation that we have adopted in our article and Section 3 presents our symplectic algorithms. We then show consistency between our simulation using GRIT and secular theories in Section 4, for the case of a moonless Earth and the case of a hypothetical Earth–Moon system that includes tidal interactions. Finally, we apply our package to simulate Trappist-I in Section 5 to investigate the effects of spin–orbit coupling in TTVs, as well as in the tidally synchronized states of Trappist-I planets.

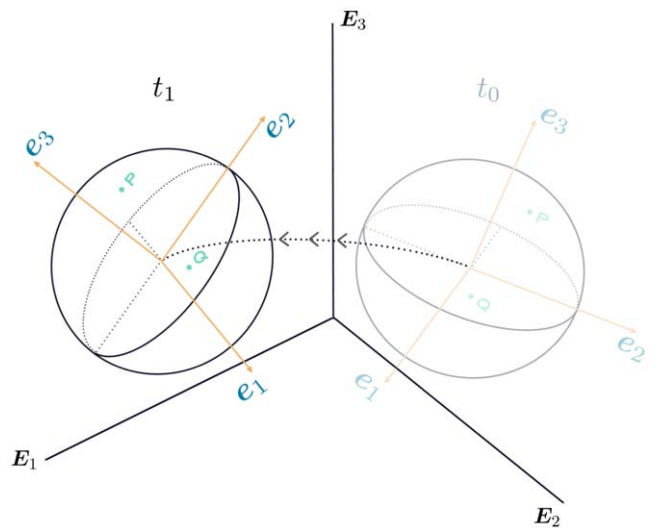


Figure 1. The body frame.

2. Rigid Body Representation

Given that we are interested in the dynamics of the planet’s spin axis, the planet is modeled as a rigid body to account for its finite size and rotation. Other than the spatial position and the linear momentum, the rotational orientation and angular momentum of the rigid body are necessary to represent its state. The above are 12-dimensional in total, and besides the spatial position (3-dim) and its conjugate linear momentum (3-dim), we still need a set of variables (6-dim) to represent the orientation and the rotation of the rigid body.

2.1. The Body Frame and the Rotation Matrix

Under a specific fixed reference frame of Euclidean space \mathbb{R}^3 with basis (E_1, E_2, E_3) , the spatial position and the translational speed of a body can be expressed by vectors in \mathbb{R}^3 . Meanwhile, the body frame (Figure 1) attached to the body gives fixed coordinates of each small particle of the body. As can be seen from Figure 1, orthogonal bases (e_1, e_2, e_3) form a body frame of this rigid body. As the body moves along the dashed trajectory following the arrows, as well as self rotating from time t_0 to time t_1 , the coordinates of points P, Q under the body frame stay the same, without being subject to the motion of the rigid body.

The configuration of a rigid body is described by both the position of its center of mass and its rotational orientation. The orientation in the reference frame can be expressed as a rotation by an orthogonal matrix $\mathbf{R}(t) \in \text{SO}(3)$ from the body frame (e.g., z-axis of the body frame at time t will be $\mathbf{R}(t) \cdot [0 \ 0 \ 1]^T$ in the reference frame). To switch between the inertia frame and the body frame, one can simply left multiply the rotation matrix \mathbf{R} or \mathbf{R}^{-1} . Note that $\mathbf{R} \in \text{SO}(3)$ and if a numerical method can keep \mathbf{R} exactly in this Lie group, then its inverse will be equal to its transpose; that is, $\mathbf{R}^{-1} = \mathbf{R}^T$.

2.2. The Angular Velocity and the Angular Momentum

By denoting $\boldsymbol{\Omega} = [\Omega_1 \ \Omega_2 \ \Omega_3]^T \in \mathbb{R}^3$ the angular velocity of the rigid body under the body frame, the direction of $\boldsymbol{\Omega}$ matches the rotational axis and $\|\boldsymbol{\Omega}\|_2$ represents the rotational speed. Consider a mass point $\mathbf{x} = [x_1 \ x_2 \ x_3]^T$ in one rigid body under the body frame, its speed under the body frame can

be expressed as

$$\boldsymbol{\Omega} \times \mathbf{x} = \begin{bmatrix} 0 & -\Omega_3 & \Omega_2 \\ \Omega_3 & 0 & -\Omega_1 \\ -\Omega_2 & \Omega_1 & 0 \end{bmatrix} \begin{bmatrix} x_1 \\ x_2 \\ x_3 \end{bmatrix} = \hat{\boldsymbol{\Omega}} \mathbf{x}, \quad (1)$$

where the hat-map $\hat{\cdot}$ is an isomorphism from the Lie algebra $\mathfrak{so}(3)$ to 3-by-3 skew-symmetric matrices, defined by

$$\hat{\boldsymbol{\Omega}} := \begin{bmatrix} 0 & -\Omega_3 & \Omega_2 \\ \Omega_3 & 0 & -\Omega_1 \\ -\Omega_2 & \Omega_1 & 0 \end{bmatrix}. \quad (2)$$

In addition, the inverse map of $\hat{\cdot}$ is denoted by $\check{\cdot}$.

With the angular velocity, the rotational kinetic energy of this rigid body can be expressed as

$$\mathbf{T}^{rot}(\boldsymbol{\Omega}) = \frac{1}{2} \boldsymbol{\Omega}^T \mathbf{J} \boldsymbol{\Omega} \quad (3)$$

with \mathbf{J} the (standard) moment of inertia tensor. Specifically, for an ellipsoid with semiaxes a, b, c and mass M , and by choosing the principal axes as the body frame such that x, y, z -axes matches semiaxes and taking the integral, we have the following moment of inertia tensor for a uniform density object.

$$\begin{aligned} \mathbf{J} &= \int_{\mathcal{B}} \rho(\mathbf{x}) \hat{\mathbf{x}}^T \hat{\mathbf{x}} d^3 \mathbf{x} \\ &= \begin{bmatrix} \frac{1}{5}M(b^2 + c^2) & 0 & 0 \\ 0 & \frac{1}{5}M(a^2 + c^2) & 0 \\ 0 & 0 & \frac{1}{5}M(a^2 + b^2) \end{bmatrix}. \end{aligned} \quad (4)$$

Note that one may substitute this with the principal moment of inertia directly.

Alternatively, the rotational kinetic energy can also be expressed as

$$\mathbf{T}^{rot}(\hat{\boldsymbol{\Omega}}) = \frac{1}{2} \text{Tr}[\hat{\boldsymbol{\Omega}} \mathbf{J}_d \hat{\boldsymbol{\Omega}}^T]. \quad (5)$$

with $\mathbf{J}^{(d)} = \int_{\mathcal{B}} \rho(\mathbf{x}) \mathbf{x} \mathbf{x}^T d\mathbf{x}$ (nonstandard) moment of inertia.

We also have $\mathbf{J}^{(d)} = \frac{1}{2} \text{Tr}[\mathbf{J}] \mathbf{I}_{3 \times 3} - \mathbf{J}$ ($\mathbf{J} = \text{Tr}[\mathbf{J}^{(d)}] \mathbf{I}_{3 \times 3} - \mathbf{J}^{(d)}$).

By definition, the angular momentum in the body frame is $\mathbf{P} = \mathbf{J} \boldsymbol{\Omega}$. By left multiplying the rotation matrix \mathbf{R} , the angular velocity and the angular momentum in the inertia frame are $\boldsymbol{\Omega} = \mathbf{R} \boldsymbol{\Omega}$ and $\mathbf{P} = \mathbf{R} \mathbf{P}$ respectively.

2.3. The Relation between the Rotation Matrix and the Angular Velocity

Express $\mathbf{R}(t) = [\mathbf{c}_1(t) | \mathbf{c}_2(t) | \mathbf{c}_3(t)]$ where $\mathbf{c}_1(t), \mathbf{c}_2(t), \mathbf{c}_3(t)$ are columns of $\mathbf{R}(t)$. We have $\mathbf{c}_1(t), \mathbf{c}_2(t), \mathbf{c}_3(t)$ representing directions of three axes of the body in the reference frame, respectively. By the definition of angular velocity, we have $\dot{\mathbf{c}}_i(t) = \hat{\boldsymbol{\Omega}} \mathbf{c}_i(t)$ for $i = 1, 2, 3$, thus

$$\dot{\mathbf{R}}(t) = \hat{\boldsymbol{\Omega}} \mathbf{R}(t). \quad (6)$$

By multiplying both sides of Equation (6) with $\mathbf{R}(t)^T$, we have $\dot{\mathbf{R}}(t) \mathbf{R}(t)^T = \hat{\boldsymbol{\omega}}$, which is a skew-symmetric matrix. Considering

the speed of an arbitrary mass point $\mathbf{x}, \mathbf{v}_x = \mathbf{R} \hat{\boldsymbol{\Omega}} \mathbf{x} = \hat{\boldsymbol{\omega}}[\mathbf{R} \mathbf{x}]$. Thus $\mathbf{R} \hat{\boldsymbol{\Omega}} = \hat{\boldsymbol{\omega}} \mathbf{R}$, which implies $\hat{\boldsymbol{\Omega}} = \mathbf{R}^T \hat{\boldsymbol{\omega}} \mathbf{R} = \mathbf{R}^T \dot{\mathbf{R}}$.

To summarize, the angular velocity and angular momentum of a rigid body in different frames are denoted as follows,

	The inertia frame (fixed)	The body frame (moving)
Angular velocity	$\boldsymbol{\omega} (= \mathbf{R} \boldsymbol{\Omega})$	$\boldsymbol{\Omega}$
Angular momentum	$\boldsymbol{\pi} (= \mathbf{R} \boldsymbol{\Pi})$	$\boldsymbol{\Pi}$

with $\boldsymbol{\Pi} = \mathbf{J} \boldsymbol{\Omega}$ and $\boldsymbol{\pi} = \mathbf{J} \boldsymbol{\omega}$. Specifically, we have $\hat{\boldsymbol{\Omega}} = \mathbf{R}^T \dot{\mathbf{R}}$ and $\hat{\boldsymbol{\Omega}} = \dot{\mathbf{R}} \mathbf{R}^T$.

The rotation matrix \mathbf{R} and the angular momentum $\boldsymbol{\Pi}$ will be utilized to describe a rigid body when we design an N-rigid-body integrator later (further details can be found in Section 3).

3. Rigid Body Simulation: Algorithms

In this section, we will design symplectic integrators of the N-rigid-body system using splitting methods. The splitting method basically views the Hamiltonian (Equation (8)) as the sum of several integrable parts. It then composes the flow of each part over some predesigned time duration to achieve a certain order of local error. In the following, we will introduce the Hamiltonian, build the symplectic integrators and analyze the accuracy of integrators step by step. In addition, we will provide a way to incorporate non-conservative forces into the integrators, such as the tidal force and post-Newtonian effects.

3.1. The Constrained Hamiltonian of an N-rigid-body System

The mass of the i th body is denoted by m_i ; $\mathbf{q}_i \in \mathbb{R}^3$ denotes the position of the i th body; $\mathbf{p}_i \in \mathbb{R}^3$ denotes the linear momentum of the i th body; $\mathbf{R}_i \in \text{SO}(3)$ denotes the rotation matrix of the i th body; $\boldsymbol{\Pi}_i \in \mathbb{R}^3$ denotes the angular momentum of the i th body; and $\mathbf{J}_i \in \mathbb{R}^{3 \times 3}$ denotes the (standard) moment of inertia tensor for the i th body.

The Hamiltonian of this system consists of the linear kinetic energy $T^{\text{linear}} = \sum_i \frac{1}{2} \mathbf{p}_i^T \mathbf{p}_i / m_i$, the rotational kinetic energy $T^{\text{rot}} = \sum_i \frac{1}{2} \boldsymbol{\Pi}_i^T \mathbf{J}_i^{-1} \boldsymbol{\Pi}_i$ and the potential energy

$$V(\mathbf{q}, \mathbf{R}) = \sum_{i < j} V_{ij}(\mathbf{q}_i, \mathbf{q}_j, \mathbf{R}_i, \mathbf{R}_j). \quad (7)$$

Denote $\mathbf{q} = \{\mathbf{q}_1, \mathbf{q}_2, \dots, \mathbf{q}_N\}$, $\mathbf{p} = \{\mathbf{p}_1, \mathbf{p}_2, \dots, \mathbf{p}_N\}$, $\boldsymbol{\Pi} = \{\boldsymbol{\Pi}_1, \boldsymbol{\Pi}_2, \dots, \boldsymbol{\Pi}_N\}$, $\mathbf{R} = \{\mathbf{R}_1, \mathbf{R}_2, \dots, \mathbf{R}_N\}$. The Hamiltonian can be expressed as

$$\begin{aligned} H(\mathbf{q}, \mathbf{p}, \boldsymbol{\Pi}, \mathbf{R}) &= \sum_i \frac{1}{2} \mathbf{p}_i^T \mathbf{p}_i / m_i \\ &+ \sum_i \frac{1}{2} \boldsymbol{\Pi}_i^T \mathbf{J}_i^{-1} \boldsymbol{\Pi}_i + V(\mathbf{q}, \mathbf{R}) \text{ with } \mathbf{R}_i \in \text{SO}(3). \end{aligned} \quad (8)$$

The true potential energy between i th body and j th body is

$$\int_{\mathcal{B}_i} \int_{\mathcal{B}_j} -\frac{\mathcal{G} \rho(\mathbf{x}_i) \rho(\mathbf{x}_j)}{\|(\mathbf{q}_i + \mathbf{R}_i \mathbf{x}_i) - (\mathbf{q}_j + \mathbf{R}_j \mathbf{x}_j)\|} d\mathbf{x}_j d\mathbf{x}_i. \quad (9)$$

We may approximate this as V_{ij} (in Equation (7)) by Taylor expanding the denominator. By expanding to the 2nd order with respect to the radius of the planet over the distance

between two bodies (see Appendix A), the approximated potential is,

$$\begin{aligned} & \int_{\mathcal{B}_i} \int_{\mathcal{B}_j} -\frac{\mathcal{G}\rho(\mathbf{x}_i)\rho(\mathbf{x}_j)}{\|(\mathbf{q}_i + \mathbf{R}_i \mathbf{x}_i) - (\mathbf{q}_j + \mathbf{R}_j \mathbf{x}_j)\|} d\mathbf{x}_j d\mathbf{x}_i \\ & \approx -\frac{\mathcal{G}m_i m_j}{\|\mathbf{q}_i - \mathbf{q}_j\|} - \frac{\mathcal{G}(m_i \text{Tr}[\mathbf{J}_i] + m_j \text{Tr}[\mathbf{J}_j])}{2 \|\mathbf{q}_i - \mathbf{q}_j\|^3} \\ & + \frac{3\mathcal{G}(\mathbf{q}_i - \mathbf{q}_j)^T (m_j \mathbf{R}_i \mathbf{J}_i \mathbf{R}_i^T + m_i \mathbf{R}_j \mathbf{J}_j \mathbf{R}_j^T)(\mathbf{q}_i - \mathbf{q}_j)}{2 \|\mathbf{q}_i - \mathbf{q}_j\|^5} \end{aligned} \quad (10)$$

with $-\frac{\mathcal{G}m_i m_j}{\|\mathbf{q}_i - \mathbf{q}_j\|}$ being the potential of purely point-mass interactions and the rest being the corrections of the potential due to the body i and j not being point masses. If we further expand the potential to the 4th order (see Appendix A), then rigid-body rigid-body interactions will also be included as higher order corrections. For example, fourth order potential has recently been considered for binary asteroids with large non-spherical terms, and leads to interesting effects (Hou et al. 2017).

3.2. Equations of Motion

The Lagrangian for a system consisting of one rigid body is a function of $\mathbf{R}(t)$ and $\dot{\mathbf{R}}(t)$ by plugging in $\hat{\Omega} = \mathbf{R}^T \dot{\mathbf{R}}$ in Equation (5),

$$L(\mathbf{R}, \dot{\mathbf{R}}) = \frac{1}{2} \text{Tr}[\dot{\mathbf{R}} \mathbf{J}_d \dot{\mathbf{R}}^T] - V(\mathbf{R}). \quad (11)$$

By utilizing the constraint $\mathbf{R}^T \mathbf{R} - \mathbf{I} = \mathbf{0}$ (Appendix B.1) or using the variational principle of Hamilton's for Lie group (Appendix B.2), one can derive the equations of motion

$$\begin{cases} \dot{\mathbf{R}} = \widehat{\mathbf{R} \mathbf{J}^{-1} \Pi}, \\ \dot{\Pi} = \Pi \times \mathbf{J}^{-1} \Pi - \left(\mathbf{R}^T \frac{\partial V(\mathbf{R})}{\partial \mathbf{R}} - \left(\frac{\partial V(\mathbf{R})}{\partial \mathbf{R}} \right)^T \mathbf{R} \right)^\vee. \end{cases} \quad (12)$$

Similarly, the equations of motion of the N-rigid-body system for the Hamiltonian (Equation (8)) are,

$$\begin{cases} \dot{\mathbf{q}}_i = \frac{\mathbf{p}_i}{m_i}, \\ \dot{\mathbf{p}}_i = -\frac{\partial V}{\partial \mathbf{q}_i}, \\ \dot{\mathbf{R}}_i = \widehat{\mathbf{R}_i \mathbf{J}_i^{-1} \Pi_i}, \\ \dot{\Pi}_i = \Pi_i \times \mathbf{J}_i^{-1} \Pi_i - \left(\mathbf{R}_i^T \frac{\partial V}{\partial \mathbf{R}_i} - \left(\frac{\partial V}{\partial \mathbf{R}_i} \right)^T \mathbf{R}_i \right)^\vee. \end{cases} \quad (13)$$

3.3. Splitting Methods for the System with Axis-symmetric Bodies

In this section, we utilize the splitting method to construct symplectic integrators. A diverse range of symplectic integrators with different accuracies and time complexities can be designed because the splitting method is quite flexible in terms of splitting and composition. Based on our Hamiltonian of the N-rigid-body system, we will explore three different types of integrators. One integrator splits the

Hamiltonian into two parts with comparable size, the other two integrators split the Hamiltonian into, respectively, three and four parts corresponding to various magnitudes and hence different timescales.

In terms of the shape of rigid bodies, we make the axis-symmetric assumption in this section for simplicity; that is,

without loss of generality, $\mathbf{J}_i = \begin{bmatrix} \mathbf{J}_i^{(1)} & 0 & 0 \\ 0 & \mathbf{J}_i^{(1)} & 0 \\ 0 & 0 & \mathbf{J}_i^{(3)} \end{bmatrix}$. Different splitting mechanisms can be applied for general rigid bodies that are not axis-symmetric (see Section 3.5).

3.3.1. Classical Splitting for Rigid Body: $H = H_1 + H_2$ with $\frac{H_1}{H_2} = \mathcal{O}(1)$

One way of splitting is $H = H_1 + H_2$ following Dullweber et al. (1997), with

$$\begin{cases} H_1(\mathbf{q}, \mathbf{p}, \Pi, \mathbf{R}) = \sum_i \frac{1}{2} \mathbf{p}_i^T \mathbf{p}_i / m_i + \sum_i \frac{1}{2} \Pi_i^T \mathbf{J}_i^{-1} \Pi_i, \\ H_2(\mathbf{q}, \mathbf{p}, \Pi, \mathbf{R}) = V(\mathbf{q}, \mathbf{R}) = \sum_{i \neq j} V_{ij}(\mathbf{q}_i, \mathbf{q}_j, \mathbf{R}_i, \mathbf{R}_j). \end{cases} \quad (14)$$

For H_1 , the equations of motion are

$$\begin{cases} \dot{\mathbf{q}}_i = \frac{\mathbf{p}_i}{m_i}, \\ \dot{\mathbf{p}}_i = 0, \\ \dot{\mathbf{R}}_i = \widehat{\mathbf{R}_i \mathbf{J}_i^{-1} \Pi_i}, \\ \dot{\Pi}_i = \Pi_i \times \mathbf{J}_i^{-1} \Pi_i. \end{cases} \quad (15)$$

In Equation (15), the 4th equation is the Euler equation for a free rigid body. This is exactly solvable, and the solution expression is particularly simple for axial-symmetric bodies:

$$\Pi_i(t) = \exp\left(-\theta t \begin{bmatrix} 0 \\ 0 \\ 1 \end{bmatrix}\right) \Pi_i(0) := R_z^T(\theta t) \Pi_i(0) \quad (16)$$

with $\theta = \left(\frac{1}{\mathbf{J}_i^{(3)}} - \frac{1}{\mathbf{J}_i^{(1)}}\right) \Pi_i^T(0) \begin{bmatrix} 0 \\ 0 \\ 1 \end{bmatrix}$ and R_z being the rotation matrix. Take $\Pi_i(t)$ back to the 3rd equation of Equation (15), we can also obtain $\mathbf{R}_i(t)$.

Therefore, the flow $\phi_t^{(1)}$ of H_1 is,

$$\begin{cases} \mathbf{q}_i(t) = \mathbf{q}_i(0) + \frac{\mathbf{p}_i}{m_i} t, \\ \mathbf{p}_i(t) = \mathbf{p}_i(0), \\ \mathbf{R}_i(t) = \mathbf{R}_i(0) R_{\Pi(0)} \left(\frac{\|\Pi(0)\|}{\mathbf{J}_i^{(1)}} t \right) R_z(\theta t), \\ \Pi_i(t) = R_z^T(\theta t) \Pi(0), \end{cases} \quad (17)$$

with R_z and $R_{\Pi(0)}$ being rotation matrices representing the rotations around the z -axis and $\Pi(0)$, respectively.

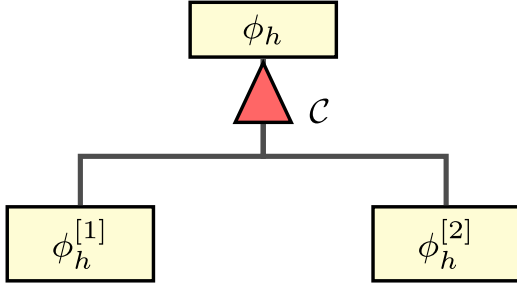


Figure 2. Composition of $\phi_h^{[1]}$ and $\phi_h^{[2]}$. The root node represent the final scheme. The leaves represent the basic ingredients of the composition, which are exact flows. The red arrow represent the composition method specialized in composing two child flows with comparable scales.

For H_2 , the equations of motion are

$$\begin{cases} \dot{\mathbf{q}}_i = 0, \\ \dot{\mathbf{p}}_i = -\frac{\partial V}{\partial \mathbf{q}_i}, \\ \dot{\mathbf{R}}_i = 0, \\ \dot{\Pi}_i = -\left(\mathbf{R}_i^T \frac{\partial V}{\partial \mathbf{R}_i} - \left(\frac{\partial V}{\partial \mathbf{R}_i}\right)^T \mathbf{R}_i\right)^{\vee}. \end{cases} \quad (18)$$

Because \mathbf{q}_i and \mathbf{R}_i stay constant, we have \mathbf{p}_i and Π_i changing at constant rates. Therefore, the flow $\phi_t^{[2]}$ for H_2 is given by

$$\begin{cases} \mathbf{q}_i(t) = \mathbf{q}_i(0), \\ \mathbf{p}_i(t) = \mathbf{p}_i(0) - \frac{\partial V}{\partial \mathbf{q}_i} t, \\ \mathbf{R}_i(t) = \mathbf{R}_i(0), \\ \Pi_i(t) = \Pi_i(0) - \left(\mathbf{R}_i^T \frac{\partial V}{\partial \mathbf{R}_i} - \left(\frac{\partial V}{\partial \mathbf{R}_i}\right)^T \mathbf{R}_i\right)^{\vee} t. \end{cases} \quad (19)$$

We may compose $\phi_t^{[1]}$ and $\phi_t^{[2]}$ via \mathcal{C} to construct different symplectic integrators (see, e.g., McLachlan & Quispel 2002), see Figure 2. To name a few, set \mathcal{C} as $\mathcal{C}_{\text{Euler}}$, $\phi_h = \phi_h^{[1]} \circ \phi_h^{[2]}$ is a 1st order scheme with h being the step size (see Appendix D for $\mathcal{C}_{\text{Euler}}$ and the following composition methods $\mathcal{C}_{\text{Verlet}}$ and \mathcal{C}_{S6}).

By applying symmetric composition $\mathcal{C}_{\text{Verlet}}$, a 2nd order integrator \mathcal{T}_2 is in the form of

$$\phi_h^{\text{Verlet}} := \mathcal{C}_{\text{Verlet}}(\phi_h^{[1]}, \phi_h^{[2]}) = \phi_{\frac{h}{2}}^{[1]} \circ \phi_h^{[2]} \circ \phi_{\frac{h}{2}}^{[1]} \quad (20)$$

By applying ϕ_h^{TriJump} (Suzuki 1990), we have the following 4th-order scheme \mathcal{T}_4 ,

$$\phi_{\gamma_1 h}^{\text{Verlet}} \circ \phi_{\gamma_2 h}^{\text{Verlet}} \circ \phi_{\gamma_3 h}^{\text{Verlet}}, \quad (21)$$

with $\gamma_1 = \gamma_3 = \frac{1}{2 - 2^{1/3}}$, $\gamma_2 = 1 - 2\gamma_1$. Similarly, a 6th-order scheme \mathcal{T}_6 can be constructed by composing $\phi_h^{[1]}, \phi_h^{[2]}$ with \mathcal{C}_{S6}

In the package, \mathcal{T}_2 , \mathcal{T}_4 and \mathcal{T}_6 are implemented.

3.3.2. Tailored Splitting I: $H = H_1 + H_2 + H_3 + H_4$ with $\frac{H_1}{H_2} = \mathcal{O}(1)$ and $\frac{H_3}{H_1}, \frac{H_4}{H_2} = \mathcal{O}(\varepsilon)$

In contrast from point-mass systems, which can already exhibit dynamics over multiple timescales, the N-rigid-body system can have additional timescales created by the rotational dynamics.

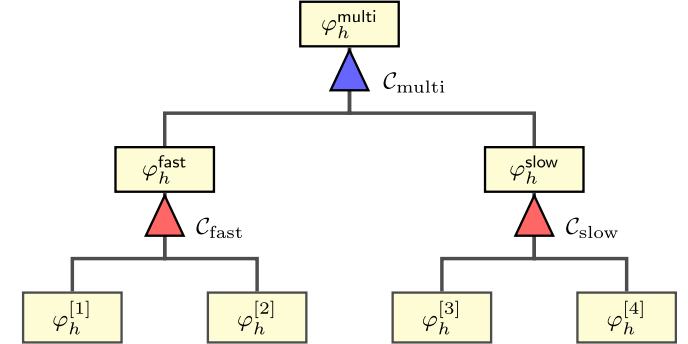


Figure 3. Hierarchical composition tree. The root node represents the final scheme. The leaves represent the basic ingredients of the composition which are exact flows. Nodes in the middle represent the intermediate composition flows. Red arrows represent the composition methods specialized in composing two child flows with similar scales. The blue arrow represent the composition methods specialized in composing two child flows with different scales.

Thus, we further split the Hamiltonian into more terms of different magnitudes, which produce flows at different timescales, and we then carefully compose them.⁴ More specifically, consider $H = H_1 + H_2 + H_3 + H_4$ with

$$\begin{cases} H_1(\mathbf{q}, \mathbf{p}) = \sum_i \frac{1}{2} \mathbf{p}_i^T \mathbf{p}_i / m_i \\ H_2(\mathbf{q}, \mathbf{p}) = -\sum_{i < j} \frac{G m_i m_j}{\|\mathbf{q}_i - \mathbf{q}_j\|}, \\ H_3(\Pi) = \sum_i \frac{1}{2} \Pi_i^T \mathbf{J}_i^{-1} \Pi_i, \\ H_4(\mathbf{q}, \mathbf{R}) = V(\mathbf{q}, \mathbf{R}) - H_2. \end{cases} \quad (22)$$

Here, H_1, H_2 have comparable size and $\frac{H_3}{H_1}, \frac{H_4}{H_2} = \mathcal{O}(\varepsilon)$, with ε being a small scaling parameter determined by the properties of the system. Based on scales of the dynamics, we denote $H^{\text{fast}} = H_1 + H_2$ and $H^{\text{slow}} = H_3 + H_4$. For example, consider the solar system, setting all the bodies to be point masses except the Earth, $\varepsilon \approx 10^{-6}$.

The flows $\{\phi_t^{[1]}, \phi_t^{[2]}, \phi_t^{[3]}, \phi_t^{[4]}\}$ of $\{H_1, H_2, H_3, H_4\}$ can be derived similarly to Section 3.3.1 and the schemes are built by hierarchically composing $\{\phi_t^{[i]}\}_{i=1}^4$ together. Specifically, as shown in Figure 3, we first group the flows of the fast dynamics ($\phi_t^{[1]}$ and $\phi_t^{[2]}$) as a sub-scheme ϕ_h^{fast} via $\mathcal{C}_{\text{fast}}$ and the flows of the slow dynamics ($\phi_t^{[3]}$ and $\phi_t^{[4]}$) as a sub-scheme ϕ_h^{slow} via $\mathcal{C}_{\text{slow}}$, respectively. Then, composing ϕ_h^{fast} and ϕ_h^{slow} together as the final scheme ϕ_h^{multi} via $\mathcal{C}_{\text{multi}}$. $\mathcal{C}_{\text{fast}}$ and $\mathcal{C}_{\text{slow}}$ are composition methods of composing two Hamiltonian flows with comparable scales (McLachlan & Quispel 2002). $\mathcal{C}_{\text{multi}}$ is a composition method that is specialized in perturbative Hamiltonian systems of the form $H = A + \varepsilon B$ (McLachlan 1995; Laskar & Robutel 2001; Blanes et al. 2013). Note that the flows ϕ_h^{fast} , ϕ_h^{slow} are not exact, so the order of ϕ_h^{multi} is not the same as the order of $\mathcal{C}_{\text{multi}}$ applied for exact flows. In fact, the global error of ϕ_h^{multi} is the summation of the global errors of all three methods $\mathcal{C}_{\text{fast}}$, $\mathcal{C}_{\text{slow}}$ and $\mathcal{C}_{\text{multi}}$ (see Appendix C for the proof).

For example, if we set $\mathcal{C}_{\text{fast}}$, $\mathcal{C}_{\text{slow}}$ and $\mathcal{C}_{\text{multi}}$ as \mathcal{C}_{S6} , $\mathcal{C}_{\text{Verlet}}$ and $\mathcal{C}_{\text{ABA42}}$ (see Appendix D), respectively. The global error of the

⁴ Similar techniques have already been employed; see, for example, Blanes et al. (2013) and the references therein. However, the structure of our system is new (due to the rigid-body part) and thus so is our specific splitting.

Table 1

Comparisons of Different Schemes with Respect to the Number of Dominating Expensive Stages and the Global Error Order

Scheme	Expensive Stages	Order
T_2	3	(2)
T_4	7	(4)
T_6	15	(6)
\mathcal{M}_{42}	3	(4, 2)
\mathcal{M}_{642}	6	(6, 4, 2)

Note. The number of expensive stages are counted in an isolated step without considering the concatenation of the last stage with the first stage of the next step. The notation in the “order” column is explained in the main text.

above method is $\mathcal{O}(h^6) + \mathcal{O}(\varepsilon^2 h^2) + \mathcal{O}(\varepsilon h^4 + \varepsilon^2 h^2)$, i.e., $\mathcal{O}(h^6 + \varepsilon h^4 + \varepsilon^2 h^2)$. We name this the \mathcal{M}_{642} scheme with 6, 4, 2 representing the power of h of each term in the order and \mathcal{M} representing multiscale splitting.

Similarly, we design the \mathcal{M}_{42} scheme by choosing $\mathcal{C}_{\text{fast}}$, $\mathcal{C}_{\text{slow}}$ and $\mathcal{C}_{\text{multi}}$ as $\mathcal{C}_{\text{TriJump}}$, $\mathcal{C}_{\text{Verlet}}$ and $\mathcal{C}_{\text{ABA22}}$, respectively, with the global error being $\mathcal{O}(h^4 + \varepsilon h^2)$.

Compared with schemes in Section 3.3.1, tailored splitting is able to mix the fast and slow flows flexibly, and thus is able to control the time complexity. In fact, $T(\phi_h^{[1]}) = T(\varphi_h^{[1]}) + T(\varphi_h^{[3]})$, $T(\phi_h^{[2]}) = T(\varphi_h^{[2]}) + T(\varphi_h^{[4]})$ with $T(\cdot)$ being the number of operations of the one-step forward flow and evolving $\varphi_h^{[3]}$, $\varphi_h^{[4]}$ are much more expensive than evolving $\varphi_h^{[1]}$, $\varphi_h^{[2]}$. Meanwhile, $\varphi_h^{[3]}$ and $\varphi_h^{[4]}$ are (expensive) slow dynamics that can be evolved with less effort (e.g., larger step size, less stages) than fast dynamics when evolving together and tailored splitting makes it possible to control the number of expensive stages. To compare, the number of expensive stages and the global errors of all schemes mentioned (in Section 3.3.1 and Section 3.3.2) are listed in Table 1. In Table 1, the order index (o_0, o_1, \dots) represents the power of h in front of $\varepsilon^0, \varepsilon^1, \dots$ (e.g., a scheme of order (o_0, o_1, o_2) has a global error of $\mathcal{O}(h^{o_1} + \varepsilon h^{o_2} + \varepsilon^2 h^{o_3})$).

Moreover, since the hierarchical composition is a general framework, one can easily extend the family of numerical schemes, such as to construct higher order schemes, by applying a variety of existing splitting and composition methods.

3.3.3. Tailored Splitting II: $H = K_1 + K_2 + K_3$ with $\frac{K_3}{K_1}, \frac{K_2}{K_1} = \mathcal{O}(\varepsilon_K)$

We also provide an option to use the popular Wisdom-Holman (Wisdom & Holman 1991) scheme for the orbital part, which works well for the specific but common setup of near-Keplerian orbits. These systems usually correspond to $N - 1$ well-separated bodies orbiting around a massive central body (indexed by 1 in our following description). This method is similar to the approach by Touma & Wisdom (1994), except that their coordinates are set using the body frame and we provided a higher-order implementation.

By isolating the Keplerian dynamics as K_1 , combining the rotational kinetic energy with the rest translational kinetic energy as K_2 , and putting the rest potential energy to K_3 ,

$H = K_1 + K_2 + K_3$ with

$$\begin{cases} K_1(\mathbf{q}, \mathbf{p}) = H_{\text{Kepler}}(\mathbf{Q}, \mathbf{P}) = \sum_{i=2}^N \frac{1}{2} \mathbf{P}_i^T \mathbf{P}_i / m_i - \frac{G m_1 m_i}{\|\mathbf{Q}_i\|}, \\ K_2(\mathbf{p}, \Pi) = \sum_{i=1}^N \frac{1}{2} \mathbf{\Pi}_i^T \mathbf{J}_i^{-1} \mathbf{\Pi}_i + \frac{\left\| \mathbf{p}_1 - \frac{m_1}{m_{\text{tot}}} \sum_{i=1}^N \mathbf{p}_i \right\|^2}{2m_1}, \\ K_3(\mathbf{q}, \mathbf{R}) = V(\mathbf{q}, \mathbf{R}) + \sum_{i=2}^N \frac{G m_1 m_i}{\|\mathbf{q}_i - \mathbf{q}_1\|}, \end{cases} \quad (23)$$

and $K_2, K_3 \ll K_1$. Here, $V(\mathbf{q}, \mathbf{R})$ is defined in Equation (7). Note that K_1 represents Keplerian orbits in \mathbf{Q}, \mathbf{P} variables, which are canonical democratic heliocentric variables (Duncan et al. 1998) with

$$\mathbf{Q}_i = \begin{cases} \mathbf{q}_i - \mathbf{q}_1 & i \neq 1, \\ \frac{\sum_{j=1}^N m_j \mathbf{q}_j}{m_{\text{tot}}} & i = 1, \end{cases} \quad (24)$$

and

$$\mathbf{p}_i = \begin{cases} \mathbf{p}_i - \frac{m_i}{m_{\text{tot}}} \sum_{j=1}^N \mathbf{p}_j & i \neq 1, \\ \sum_{j=1}^N \mathbf{p}_j & i = 1. \end{cases} \quad (25)$$

So when evolving K_1 dynamics, additional steps of switching back and forth between (\mathbf{q}, \mathbf{p}) and (\mathbf{Q}, \mathbf{P}) coordinates are necessary. In terms of compositions, similarly, we first compose the flows of K_2 and K_3 together as $\varphi_h^{K, \text{slow}}$ via $\mathcal{C}_{\text{slow}}^K$, we then compose the flow of K_1 ($\varphi_h^{K, \text{fast}}$) with $\varphi_h^{K, \text{slow}}$ via a multiscale compositing method $\mathcal{C}_{\text{multi}}^K$. The error of this composition is the summation of the global errors of two methods $\mathcal{C}_{\text{slow}}^K, \mathcal{C}_{\text{multi}}^K$ (and the numerical error of evolving Keplerian orbits).

For instance, \mathcal{K}_2 method in our package is based on choosing $\mathcal{C}_{\text{slow}}^K, \mathcal{C}_{\text{multi}}^K$ as $\mathcal{C}_{\text{Verlet}}$ and $\mathcal{C}_{\text{ABA22}}$, and its global error is $\mathcal{O}(\varepsilon_K h^2)$.

3.3.4. Which One to Use, the \mathcal{T} -series, the \mathcal{M} -series, or the \mathcal{K} -series Methods?

In general, the orders of the \mathcal{T} -series methods are only h dependent, while the \mathcal{M} -series and \mathcal{K} -series methods are (h, ε) dependent and (h, ε_K) dependent, respectively. Here, ε and ε_K are system specific, and they affect the choice of method. For example, $\varepsilon \approx 10^{-6}$ and $\varepsilon_K \approx 10^{-3}$ in Solar system simulations with Earth being the only rigid body—note that ε_K represents the scale of the orbital planetary interactions while the ε in Section 3.3.2 represents the scale of the spin and the potential correction due to rigidity, so in practice, $\varepsilon \ll \varepsilon_K$. With the small parameters incorporated, the tailored splitting methods are usually more efficient. In general, the \mathcal{K} -series methods specialize in near-Keplerian problems, while the \mathcal{M} -series methods are more generic and at the same time almost always faster than the \mathcal{T} -series methods with nearly no trade-offs of the accuracy. In fact, the \mathcal{M} -series methods are often both more

accurate and more efficient, due to delicate splittings and compositions⁵. However, T -series methods are recommended for extreme cases with large ε and ε_K (e.g., a super fast spinning body might contribute to a large ε).

3.4. Adding Non-Conservative Forces

Non-conservative forces such as tidal forces and post-Newtonian corrections are incorporated in the package. Because the implemented schemes are based on symmetric splitting and composition, the corresponding non-conservative momentum update is inserted in the middle of the composition. This is similar to how dissipative forces were added in REBOUNDx (Tamayo et al. 2020).

3.4.1. Tidal Forces

We model the tidal dissipation between each pair of bodies using the constant time lag equilibrium tide model, following Hut (1981), Eggleton et al. (1998). Note that we only adopted the dissipative component in the tidal force here. The expression of the acceleration of the tidal force is

$$\begin{aligned} \mathbf{a}_{\text{host,guest}}^{\text{tidal}} = & -\frac{9\sigma m_{\text{guest}}^2 A^2}{2\mu_{\text{host,guest}} d^{10}} [3\mathbf{d}(\mathbf{d} \cdot \dot{\mathbf{d}}) \\ & + ((\mathbf{d} \times \dot{\mathbf{d}}) - \omega d^2) \times \mathbf{d}]. \end{aligned} \quad (26)$$

Here, m_{host} , m_{guest} denote the masses of the host and the guest body, respectively; $\mathbf{d} = \mathbf{q}_{\text{guest}} - \mathbf{q}_{\text{host}}$ denotes the relative position of the guest body; $d = \|\mathbf{d}\|$ denotes the distance between two bodies; $\mu_{\text{host,guest}} = \frac{m_{\text{host}} m_{\text{guest}}}{m_{\text{host}} + m_{\text{guest}}}$ denotes the reduced mass; ω denotes the angular velocity of the host body under the reference frame (the inertia frame); the constant σ denotes the dissipation rate; A is defined as

$$A = \frac{d^5 Q}{1 - Q}, \quad (27)$$

with Q the constant that measures quadrupolar deformability of the objects.

The dissipation rate σ is related to the time lag τ by the following formula,

$$\tau = \frac{3\sigma d^5}{4G} \cdot \frac{Q}{1 - Q}. \quad (28)$$

We may integrate the tidal acceleration $\mathbf{a}_{i,j}^{\text{tidal}}$ to our integrator after each time step by considering all pairs of bodies under tidal interactions. Note that each $\mathbf{a}_{i,j}^{\text{tidal}}$ only calculates the force of each (host, guest) pair, where each pair (i, j) treat i as the extended object and j as the point-mass object. Thus, the equations of motion due to tidal dissipation are listed below:

$$\begin{cases} \mathbf{p}_i = \mathbf{p}_i + h \sum_{j \neq i} (-\mu_{i,j} \mathbf{a}_{i,j}^{\text{tidal}} + \mu_{j,i} \mathbf{a}_{j,i}^{\text{tidal}}), \\ \mathbf{\Pi}_i = \mathbf{\Pi}_i - h \sum_{j \neq i} \mu_{i,j} \mathbf{R}_i^T ((\mathbf{q}_j - \mathbf{q}_i) \times \mathbf{a}_{i,j}^{\text{tidal}}). \end{cases} \quad (29)$$

⁵ One should not be misled to think that an error like $\mathcal{O}(h^4 + \varepsilon h^2)$ is larger than $\mathcal{O}(h^4)$; for example, if $\varepsilon = h^2$, the former may actually be smaller due to different constant factors; see Section 4.1.3 for practical illustrations.

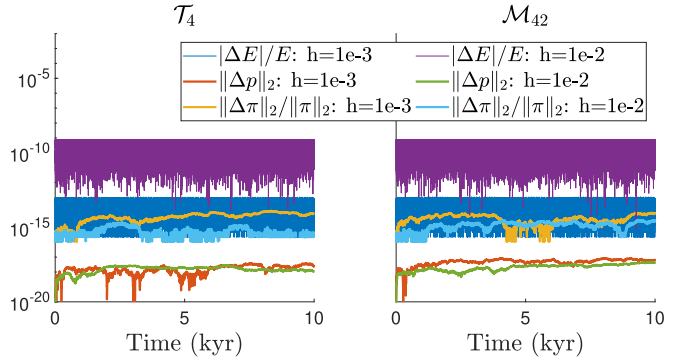


Figure 4. Conservation of momentum maps and near conservation of energy by our methods. Relative error of energy E , error of the total linear momentum \mathbf{p} and relative error of the total angular momentum π are measured. $\mathbf{p}(0) = [0, 0, 0]$. The potential order is set to 2.

3.4.2. General Relativistic Effects

We added the first-order post-Newtonian correction for general relativistic effects following (for example) Blanchet (2006). For planetary systems, we assumed that the central object (the host star) is much more massive when compared to the surrounding objects (the planets). Thus, we only included the correction due to the star. The acceleration can be expressed as follows (e.g., Anderson et al. 1975; Benitez & Gallardo 2008):

$$\mathbf{a} = \frac{GM_{\text{star}}}{r^3 c^2} \left[\left(\frac{4GM_{\text{star}}}{r} - \mathbf{v}^2 \right) \mathbf{r} + 4(\mathbf{v} \cdot \mathbf{r}) \mathbf{v} \right] \quad (30)$$

3.5. Asymmetric Case

For planets with close-in orbits, both rotational flattening and tidal force distort the shape of the planets, and lead to non-axial symmetric distortions. Thus, we include the option to study non-axial symmetric planets here, where one could specify the principal moment of inertia or the semiaxes of the planets directly. In this case, $J_i^{(1)} \neq J_i^{(2)} \neq J_i^{(3)}$ in \mathbf{J}_i , and our splitting of the Hamiltonian is modified as the previous Hamiltonian plus $H_{\text{asymmetric}}$, where

$$H_{\text{asymmetric}}(\mathbf{R}, \Pi) = \sum_i \left(\frac{1}{J_i^{(2)}} - \frac{1}{J_i^{(1)}} \right) \cdot \frac{\Pi_i^{(2)}{}^2}{2}, \quad (31)$$

and $H_{\text{asymmetric}} \ll H_3$ in Equation (22).

The dynamics of Equation (31) are

$$\begin{cases} \mathbf{R}_i(t) = R_y(\delta \Pi_i^{(2)} t) \mathbf{R}_i(0), \\ \mathbf{\Pi}_i(t) = R_y(-\delta \Pi_i^{(2)} t) \mathbf{\Pi}_i(0), \end{cases} \quad (32)$$

with $\delta = \frac{1}{J_i^{(2)}} - \frac{1}{J_i^{(1)}}$. Based on the symmetric schemes in Section 3.3.2, we simply evolve $H_{\text{asymmetric}}$ half step at the beginning and the end of each step.

4. Code Validation

4.1. Numerical Tests

4.1.1. Conservation Properties

The conservation properties of the integrators are tested for T_4 and M_{42} schemes in the Sun–Earth–Moon system with all three bodies being rigid. As shown in Figure 4, both schemes

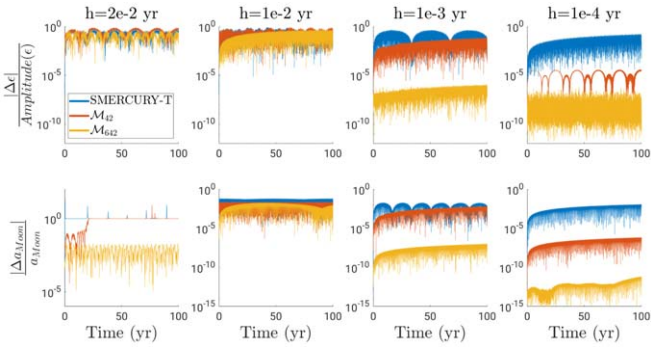


Figure 5. Error of Earth’s obliquity (ϵ) over the range of ϵ ’s fluctuation and the relative error of the semimajor axis of the Moon for the Sun–Earth–Moon system. Earth, Sun, Moon are rigid body, point mass and point mass, respectively. The benchmark is simulated using the \mathcal{T}_6 scheme with $h = 10^{-5}$ yr.

conserve linear momentum and angular momentum (except that there are arithmetic inaccuracies due to machine precision), and the energies exhibit no drift but only fluctuate at magnitudes $\mathcal{O}(h^4)$ and $\mathcal{O}(h^4 + \epsilon h^2)$ for \mathcal{T}_4 and \mathcal{M}_{42} , respectively. In the simulations, tides are not included (otherwise the system is no longer conservative) and initial conditions are set to be the data of epoch J2000 from JPL HORIZONS System.

Here, the floating-point format is set to double precision, although our package can also use long-double or single-precision.

Our integrators also (exactly) preserve symplecticity when tidal dissipation is excluded because they are Hamiltonian splitting schemes. The definition of symplecticity in a non-Euclidean setup is not completely trivial, but the symplecticity of splitting approaches considered here has been established in (for example) Tao & Ohsawa (2020) (with $r(t) = 0$; otherwise one gets a more general result, namely conformal symplecticity).

4.1.2. Convergence Tests and Accuracy Comparisons

We now numerically illustrate how the integration error depends on h for different numerical schemes, which include both the methods that we implemented in GRIT and SMERCURY-T. SMERCURY-T is a concurrent simulation package that can evolve an object’s spin axis under obliquity tide (Kreyche et al. Submitted), which is based on the Mercury simulation package (Chambers 1999). Specifically, it includes a subroutine to evolve the spin-axis dynamics following the procedure outlined in Lissauer et al. (2012), which is based on the Lie–Poisson integrator of rigid-body dynamics developed by Touma & Wisdom (1994). In addition, it includes a subroutine for obliquity tide following the algorithms outlined in Bolmont et al. (2015). The model for tidal interaction of SMERCURY-T is different from what we included in GRIT, which naturally contains both obliquity tide and tidal effects due to non-tidally synchronized orbits. Thus, we focus here on the rigid-body dynamics, where we do not include tidal interactions in our convergence test. In the comparisons presented here, we also turned off our rigid-body rigid-body interaction option (which is mainly for accurate simulations of rigid bodies’ close encounters) because these interactions are supported only in GRIT.

We first test on the Sun–Earth–Moon system (Figure 5). One observation in this case is that if the step size is too large so that

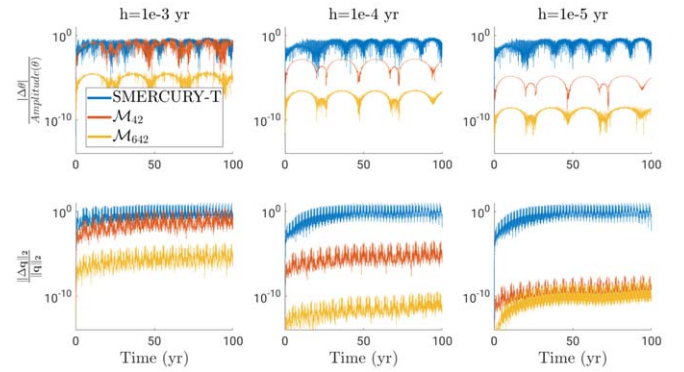


Figure 6. Error of spin angle (the angle between the angular momentum and the z -axis of the inertia frame) and position for an Earth-like planet orbiting around two stars alternatively. The Earth-like planet, star 1 and star 2 are set to be rigid body, point mass and point mass, respectively. The benchmark is simulated using the \mathcal{T}_6 scheme with $h = 1e-5$.

splitting into $H_1 + H_2 + H_3 + H_4$ (GRIT’s \mathcal{M}_{42} , \mathcal{M}_{642}) does not work, then SMERCURY-T does not work either (unlike expected by some). More precisely, with $h = 2 \cdot 10^{-2}$ yr, \mathcal{M}_{42} and SMERCURY-T cannot resolve the motion of the Moon orbiting around the Earth, whose period is a month, and even the performance of the 6th-order method \mathcal{M}_{642} is not ideal and significant errors are observed in all methods. Accuracy is improved for step sizes below this stability limit, and the rate of improvement is (as expected) dependent on the order of the numerical scheme. Consequently, higher order methods, such as \mathcal{M}_{42} and \mathcal{M}_{642} , show substantially smaller errors when smaller step sizes are applied (readers interested in understanding this together with computational costs are referred to Section 4.1.3).

We then test on a non-Keplerian system (note SMERCURY-T performs well for near-Keplerian problems as designed) using an Earth-like planet orbiting around two stars alternatively in a stellar binary system (Figure 6). Given that there is no single body that has the dominant mass of the system and the planet is alternatively captured by the two stars, the planetary orbit is not nearly Keplerian, and splitting into $H_1 + H_2 + H_3 + H_4$ is more accurate than SMERCURY-T for all choices of step size here. Specifically, as shown in Figure 6, the orbital position of SMERCURY-T saturates to $\mathcal{O}(1)$ relative error after a relatively short period of time, no matter if $h = 10^{-3}$, 10^{-4} , or 10^{-5} yr. The orbital inaccuracy naturally also affects the spin angle. Meanwhile, \mathcal{M}_{42} and \mathcal{M}_{642} do not have this issue.

For reproducibility, the initial condition used is

$$\begin{aligned} \mathbf{q}_{\text{star}_1} &= [-0.5 \ 0 \ 0]^T, \mathbf{v}_{\text{star}_1} = [0 \ -0.0086012119 \ 0]^T, \\ \mathbf{q}_{\text{star}_2} &= [0.5 \ 0 \ 0]^T, \mathbf{v}_{\text{star}_2} = [0 \ 0.0086012119 \ 0]^T, \\ \mathbf{q}_{\text{planet}} &= [1.16 \ 0 \ 0]^T, \mathbf{v}_{\text{planet}} = [0 \ 0.0164271047 \ 0]^T \end{aligned}$$

in units of au and au/day , and $m_{\text{star}_1} = m_{\text{star}_2} = 0.5m_{\odot}$, $m_{\text{planet}} = m_{\oplus}$.

4.1.3. Investigation of Efficiency

We now demonstrate the improved computational efficiency of the tailored splitting schemes. A comparison of the time efficiency among the traditional splitting method \mathcal{T}_4 , \mathcal{T}_6 and the tailored splitting scheme \mathcal{M}_{42} , \mathcal{M}_{642} , \mathcal{K}_2 in the 10 rigid body (Sun with 8 planets and the Moon) is shown in Table 2. \mathcal{M}_{42} (\mathcal{M}_{642}) is about twice the speed of \mathcal{T}_4 (\mathcal{T}_6) with comparable

Table 2
Efficiency Comparison Among Scheme T_4 , T_6 , \mathcal{M}_{42} , \mathcal{M}_{642} and \mathcal{K}_2

$h = 10^{-3}$ yr	Wall Time (s)	MAE of Earth's Obliquity
T_4	30.573	1.996646e-05
\mathcal{M}_{42}	15.488	1.997454e-05
T_6	72.55	1.728156e-08
\mathcal{M}_{642}	40.626	4.365093e-10
\mathcal{K}_2	14.673	2.186379e-05
SMERCURY-T	N/A	N/A
<hr/>		
$h = 10^{-4}$ yr		
T_4	273.71	2.680897e-09
\mathcal{M}_{42}	140.58	3.817091e-09
T_6	708.26	8.689218e-11
\mathcal{M}_{642}	395.52	2.039980e-10
\mathcal{K}_2	131.56	1.292609e-05
SMERCURY-T	N/A	N/A
<hr/>		
$h = 10^{-5}$ yr		
\mathcal{K}_2	1299.9	1.378428e-07

Note. The Solar system with eight planets and the Moon (10 rigid bodies in total) is simulated until 1000 yr with $h = 10^{-3}$ yr and $h = 10^{-4}$ yr for all schemes using a single thread. The benchmark is simulated using the T_6 scheme with $h = 10^{-5}$ yr and long-double precision. Mean absolute errors (MAE) of the Earth's obliquity (rad) are measured. Data is output every 0.1 yr.

integrating accuracy. Note that SMERCURY-T cannot be compared against here because its currently available version⁶ can only set one of the objects as a rigid-body.

To gain additional understanding of the performance of GRIT, complementary results that include comparisons to SMERCURY-T are also provided. For a fair comparison, we continue using the Solar system example, which is a near-Keplerian problem that SMERCURY-T specializes in, but we had to alter it by setting only the Earth to be a rigid body and all others as point masses. The results are given in Table 3, where \mathcal{M}_{42} shows improved accuracy over SMERCURY-T, while \mathcal{M}_{642} is even more accurate but with traded-off time complexity.

In addition, for the sake of fairness, note that wall-clock counts are platform dependent and therefore should only be used as a qualitative (not quantitative) indicator. The experiments reported here are conducted on a machine with an AMD Ryzen 7 3700X 8-Core Processor, 16 GB memory and the Linux distribution of openSUSE Leap 15.2. GRIT was compiled using GNU C++ compiler and SMERCURY-T using GNU Fortran compiler, both with the default compilation options. A single thread is used for experiments in both Tables 2 and 3 for fairness (note that a parallelization option is available in GRIT and we recommend turning it on when the simulated system has large numbers of rigid objects). We also noted that SMERCURY-T slows down more significantly than GRIT when its integration is outputted more frequently, and thus chose a large output step size to reduce SMERCURY-T's I/O overhead so that the focus can be on the integration time itself.

4.1.4. Summary of the Numerical Tests in Section 4.1

In general, GRIT suits not only near-Keplerian orbits but also non-Keplerian ones. Multiple splitting and composition

⁶ <https://github.com/SMKreyche/SMERCURY-T/tree/cbc25299825559f255cee096c7650f379af41aa5>

Table 3
Efficiency Comparison Among Scheme \mathcal{M}_{42} , \mathcal{M}_{642} and SMERCURY-T

$h = 10^{-3}$ yr	Wall Time (s)	MAE of Earth's Obliquity
\mathcal{M}_{42}	6.408	1.997119e-05
\mathcal{M}_{642}	23.122	3.841649e-10
SMERCURY-T	8.638	2.157662e-05
<hr/>		
$h = 10^{-4}$ yr		
\mathcal{M}_{42}	53.782	3.833661e-09
\mathcal{M}_{642}	216.09	1.990336e-10
SMERCURY-T	39.079	1.903458e-05

Note. The Solar system with eight planets and the Moon (nine point masses and one rigid body (the Earth) in total) is simulated until 1000 yr with $h = 10^{-3}$ yr and $h = 10^{-4}$ yr for all schemes using a single thread. The benchmark is simulated using the T_6 scheme with $h = 10^{-5}$ yr and long-double precision. Mean absolute errors (MAE) of the Earth's obliquity (rad) are measured. Data is output every 0.1 yr.

options are also provided in GRIT. Consequently, if preferred, a user can choose the classical Wisdom-Holman scheme for the orbital part, which specializes in near-Keplerian orbits (e.g., \mathcal{K}_2). Furthermore, equipped with higher order methods, GRIT integrations have errors that decrease very rapidly as step size decreases in a reasonable range.

4.2. Comparison with Secular Results

To further verify the accuracy of our integration package, we compare our simulation results to secular theory here. We include two examples: the first example integrate the obliquity variation of a moonless Earth without the influence of tidal interactions, and the second example considers tidal interactions between a hypothetical Earth–Moon system. We find good agreement between our simulation package with the results of the secular theory.

4.2.1. Obliquity Variations of a Moonless Earth

Spin-orbit resonances lead to large obliquity variations for a moonless Earth (Laskar et al. 1993). This classical example can serve as a test case for our simulation package. Specifically, planetary companions of the Earth (from Mercury to Neptune) all perturb Earth's orbit and lead to forced oscillations in the orbital plane of the Earth. At the same time, torquing from the Sun leads to precession of the Earth's spin axis. The natural precession frequency coincides with the forcing frequencies and drives resonant obliquity variations of the Earth. Tidal interactions are weak in this case, so we neglected tidal effects in our code, and consider the dynamical coupling between the planetary spin axes and its orbit.

We include the eight Solar System planets in this system, and we adopt the position and velocity of the Solar System planets from JPL database (Giorgini et al. 1996). We only treat the Earth as a rigid object with oblateness of 0.00335, and we set the other planets and the Sun as point particles.

Figure 7 shows the comparison of the obliquity variations of the moonless Earth with that from the secular theory shown in Laskar et al. (1993) and Li & Batygin (2014). We included three examples, starting with different initial obliquities, and all of them show good agreement with the secular results. In particular, below $\sim 40^\circ$, large obliquity variations can be seen, due to the spin-orbit resonances. We chose a time step of 10^{-4} yrs to

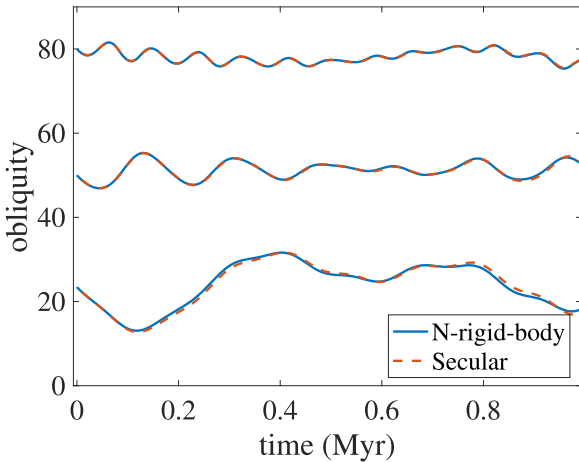


Figure 7. Obliquity variations of a moonless Earth. The solid lines represent the rigid-body simulations, and the dashed lines represent the secular results following (Laskar & Robutel 1993). The results of our simulation package agree well with the secular theory.

resolve the spin of the Earth. The fractional change in energy is of the order of 10^{-14} and the fractional change in angular momentum is of the order of 10^{-12} for all the three runs with different initial obliquities.

4.2.2. Tidal Interactions of a Hypothetical Earth–Moon System

To illustrate the accuracy of our simulation package including tidal interactions, we use a simple hypothetical Earth–Moon two-body system here. We set the initial semimajor axis and eccentricity to be 0.0018au and 0.4. For the Earth, we set the spin period to 1 day, oblateness to 0.00335, love number to 0.305 and tidal time lag to 698 sec. For the Moon, we set the spin period to 14 days, oblateness to 0.0012, love number to 0.02416 and tidal time lag to 8639 s.

Figure 8 shows the agreement between our simulation package (solid lines) with the secular results (dashed lines). The secular results are obtained following Eggleton et al. (1998). The upper panel plots orbital eccentricity versus time and the lower panel plots the spin rate of the Moon versus time. This shows that the spin rate of the Moon increases to the pseudo-synchronized state within a few hundred years, and then slowly decreases as orbital eccentricity decays due to tide. We chose a time step of 10^{-4} yr to resolve the spin of the Earth, and the total fractional change in angular momentum is 7×10^{-12} .

5. Applications to Trappist-I

Spin-orbit coupling leads to profound dynamics in planetary systems, in particular for planets with close-in orbits. For Trappist-I, it is shown that tidal and rotational deformation of the planets leads to orbital precession that can be detected in the TTV measurements (Bolmont et al. 2020). In addition, strong interactions between planets in resonant chains can push habitable zone Trappist-I planets into non-synchronous states (Vinson et al. 2019). Recently, a high accuracy differentiable N-body code for transit timing and dynamical modeling has been developed, with applications to Trappist-I, yet tidal and GR effects have not been included (Agol et al. 2021).

To illustrate the effects of the spin-orbit coupling, we use our numerical package to simulate the long-term dynamics of spin-axis variations, as well as the short-term effects on TTV

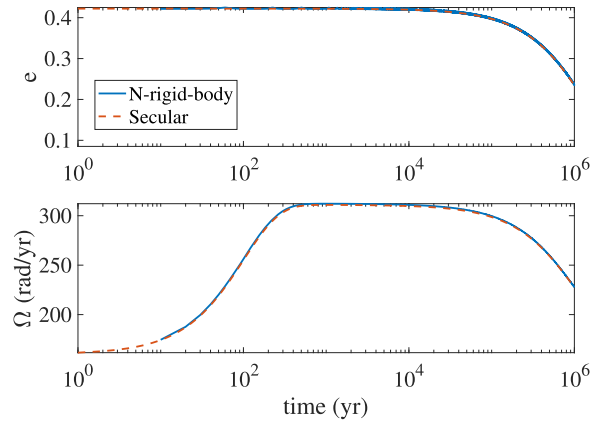


Figure 8. Tidal interaction in a hypothetical Earth–Moon system. The spin rate (Ω) increases rapidly to the pseudo-synchronized state, which is then followed by a much slower decay as the orbit circularizes under tide. The solid lines represent the simulation results and the dashed lines represent the secular results. The results of our simulation package agree well with the secular theory.

for Trappist-I. We note that both our numerical package and *POSIDONIUS* (Blanco-Cuaresma & Bolmont 2017; Bolmont et al. 2020) consider tidal effects and spin–orbit coupling, beyond point-mass dynamics based on Newtonian interactions and GR corrections. In particular, Bolmont et al. (2020) obtained both dissipative and non-dissipative forces from tidal dissipation and tidal torquing separately, and considered forcing due to planetary rotational deformation.

Using our numerical package, we find that the habitable zone planets can indeed allow large spin-state variations, consistent with the findings by Vinson et al. (2019). In addition, we find that allowing the non-synchronized states could lead to significantly larger TTVs, which could reach a magnitude of \sim min in a 10-year timescale.

5.1. System Set Up

We use the same orbital initial condition and physical properties for the planets in Trappist-I following Bolmont et al. (2020) (Table A.2 in Bolmont et al. 2020) to compare the magnitude of TTVs, and we use the same reference tidal parameters for the star and the planet (e.g., $k_{2f,*} = 0.307$, $k_{2f,p} = 0.9532$, $\Delta\tau_p = 712.37$ sec). The Q coefficient in the tidal model can then be calculated ($k_2 = Q/(1 - Q)$) (Eggleton et al. 1998; Eggleton & Kiseleva-Eggleton 2001; Fabrycky & Tremaine 2007).

To calculate the moment of inertia along the three principal axes (A , B , C), we follow the derivation by Van Hoolst et al. (2008), while assuming a homogeneous model for simplicity and assuming that the rotation velocity of the planet is close to the orbital velocity. Specifically, the moment of inertia can be expressed as follows:

$$A = I_0 \left(1 - \frac{1}{3}\alpha - \frac{1}{2}\beta\right)$$

$$B = I_0 \left(1 - \frac{1}{3}\alpha + \frac{1}{2}\beta\right)$$

$$C = I_0 \left(1 + \frac{2}{3}\alpha\right)$$

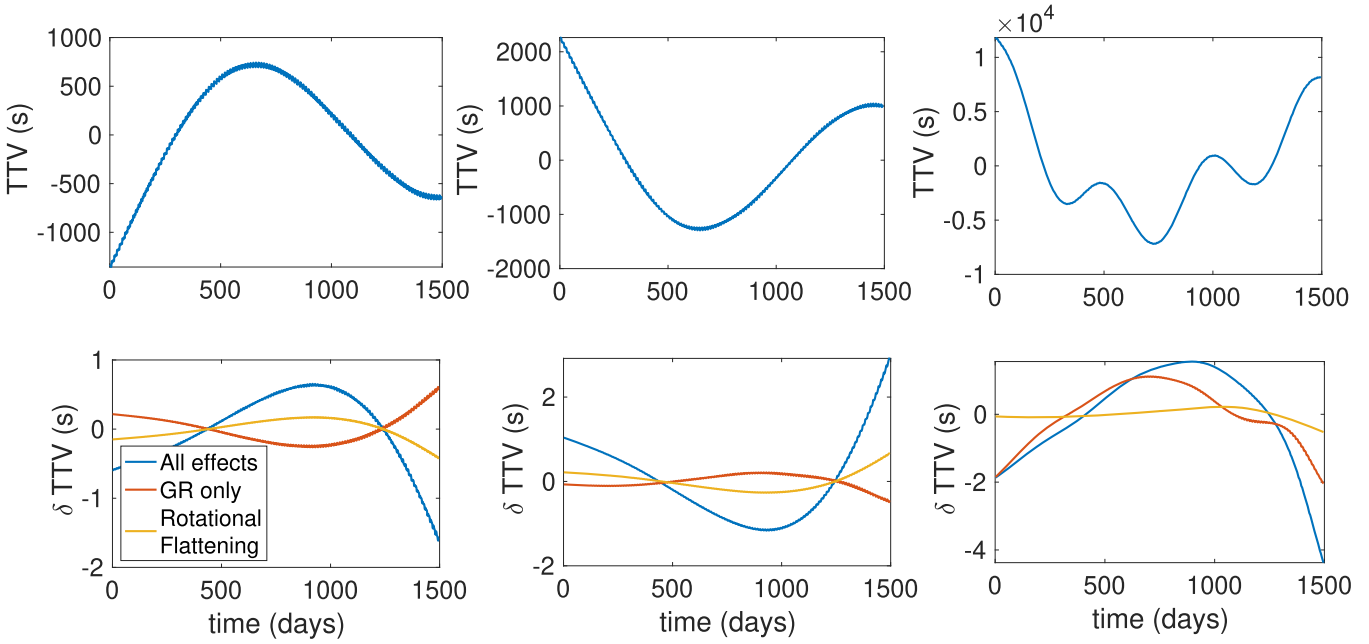


Figure 9. TTVs of planets (b, c, d) in Trappist-I. The upper panels show TTVs of the planets, assuming that they are point-mass particles and we neglect effects due to GR. The lower panels show the differences in TTVs due to GR, rotational flattening of the planets and all the effects (GR, rotational flattening, tidal precession and tidal dissipation combined). The differences due to GR and rotational flattening are consistent with the results in Bolmont et al. (2020), while assuming the planets to be rigid bodies and that the TTV differences are larger.

where

$$\alpha = \frac{5}{4}q(1 + k_f)$$

$$\beta = \frac{3}{2}q(1 + k_f)$$

and k_f is the love number, and q is the ratio of the centrifugal acceleration to the gravitational acceleration. We assume all the planets have the same radius of gyration squared $rg_p^2 = 0.3308$ following Bolmont et al. (2020), and we include in Table 4 the moment of inertia of the planets.

Moreover, because the planets are very close to their host star, general relativistic precession plays a non-negligible role in the transit time. Thus, we also included the first order post-Newtonian correction in our simulation code (see Section 3.4.2).

5.2. Transit-timing Variations

The measurement of TTVs is a powerful method to derive the physical properties of planets, in particular masses and eccentricity of planets (Agol & Fabrycky 2018). Although most studies consider only point-mass dynamics, full-body dynamics including tidal effects and distortion of the planets could also play an important role (Miralda-Escudé 2002; Heyl & Gladman 2007; Ragozzine & Wolf 2009; Maciejewski et al. 2018). It was recently shown that new measurements of the TTV of the Trappist-I system lead to significant increase in the mass estimate for planets b and c, which may be due to unaccounted physical processes including tidal effects and rotational distortion of the planets (Grimm et al. 2018; Agol et al. 2020; Bolmont et al. 2020). Thus, we use our simulation package to estimate the TTV of the inner planets in Trappist-I

Table 4
Principal Moment of Inertia of the Trappist-I Planets

Planet	A (M_{\odot} km 2)	B (M_{\odot} km 2)	C (M_{\odot} km 2)
b	50.5245	50.8474	50.955
c	54.3319	54.4432	54.4803
d	7.6321	7.6396	7.6421
e	26.384	26.391	26.3933
f	39.9836	39.9898	39.9918
g	58.8644	58.8698	58.8716
h	7.8901	7.8904	7.8905

as an example, in comparison with the study by Bolmont et al. (2020).

We include the result of the TTVs for Trappist-I b,c and d in 1500 days in Figure 9, to compare our results with those in Bolmont et al. (2020). Similar to Figure 1 in Bolmont et al. (2020), the upper panels show the TTVs assuming that the planets are all point-mass particles, and the lower panels show the differences in the TTVs due to different effects. The differences due to GR and rotational flattening of the planets computed using our simulation package are agreeable with those in Bolmont et al. (2020). In contrast to Bolmont et al. (2020), we assume the objects are rigid bodies when considering tidal interactions with the central star using our rigid-body simulator. This leads to slightly larger TTV differences. We note that the magnitude of the differences in the TTVs depend on the misalignment between the elongated principal axis and the location direction of the planet from the central star. For the illustrative example, we assume that the planets all start with their long axes perfectly aligned to the direction of the central star.

As the system evolves further, the misalignment could be excited to larger values (as discussed further in Section 5.3).

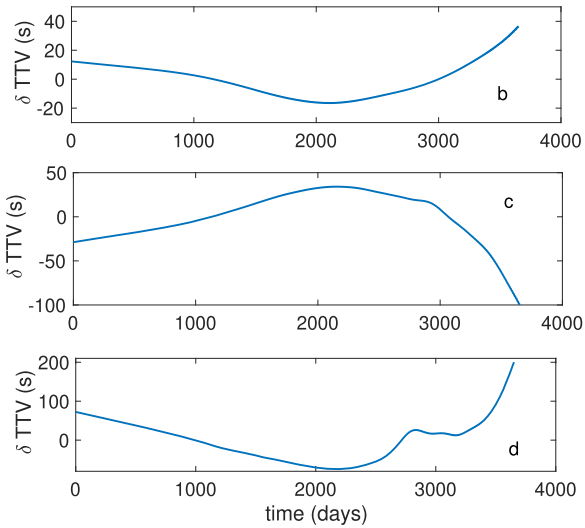


Figure 10. Differences in TTVs of planets (b, c, d) in Trappist-I over 10-year measurements. With larger spin-misalignment, TTVs could reach \sim mins.

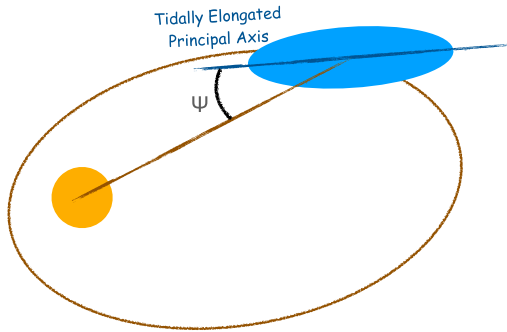


Figure 11. Illustration of the long-axis misalignment. Low variations in ψ correspond to a tidally locked planet.

The differences in TTVs could reach ~ 5 s for 1500 days, and a few minutes in 10-year measurements, as shown in Figure 10. A detailed study of how the TTVs depend on the physical properties of the planets (e.g., the love number, tidal time lag, etc.) is out of the scope of this paper, and will be discussed in a follow up project.

5.3. Long-term Dynamics

The long-term dynamics of the spin axes of planets, in particular their synchronized states, play an important role in the atmosphere circulation of the planets. When the planets are tidally locked, the extreme temperature differences on one side of the planet facing the star from the other side may lead to the collapse of the planetary atmosphere (Kasting et al. 1993; Joshi et al. 1997; Wordsworth 2015). For Trappist-I, Vinson et al. (2019) developed a framework studying the spin-axis variations of the planets and found that the mean-motion resonant chain could drive the habitable zone planets out of the synchronized state.

Specifically, Vinson et al. (2019) evolves the longitude of the substellar point separately based on results of orbital evolution of Trappist-I using the *Rebound* simulation package

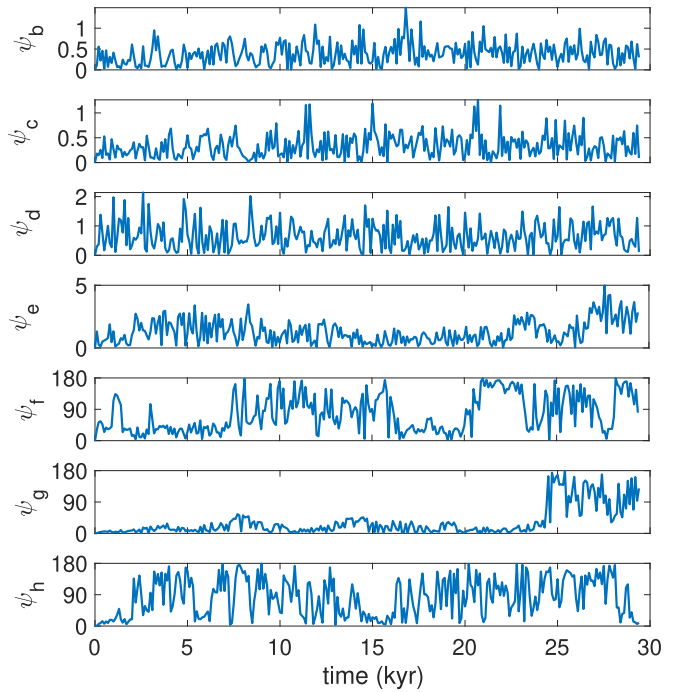


Figure 12. Spin-axis misalignment as a function of time. Planets f, g and h all have large long-axes variations, and are not tidally locked.

(Tamayo et al. 2017). This does not include effects of the variation of the spin axis on the orbits and the developed framework neglected the 3-D variations of the planetary spin axis (i.e., assuming zero planetary obliquities) for simplicity. We use our simulation package to evaluate the spin-axis dynamics more accurately, which allows backreactions of the spin-axis dynamics on the orbit, as well as the full 3-D dynamics of the planetary spin axis.

We use the same initial condition as those in Section 5.2 for the long-term dynamical simulation over 100,000 yr. We start the planets in synchronized configurations, and we calculate the misalignment between the long axes of the planets and their radial direction from the host star. ψ is illustrated in Figure 11.

Figure 12 shows this misalignment (ψ) of the planets. Planets b, c, d and e are closer to the host star, and allow stronger tidal interactions. This leads to low variations in the long axes of the planets. However, planets f, g and h are further away, where planetary interactions could compete with tidal realignment and drive larger spin-axis variations. We note that the obliquities of these planets still remain low (within a few degrees). The detailed dependence of the spin-axis variations on the parameters of the planets are beyond the scope of this article, and will be invested in a follow up paper.

6. Conclusions

In this article, we developed symplectic integrators and provided a package “GRIT” to study the spin-orbit coupling of N-rigid-body systems. We split the Hamiltonian into four parts with different evolution timescales (tailored splitting), and we compose the four parts hierarchically so that the expensive slow scale evolution is more efficient. In general, tailored splitting is more flexible and efficient than traditional splitting.

To illustrate the validity of the integrator, we showed that it provides results that are consistent with the secular theories for the obliquity variation of a moonless Earth, and the tidal evolution of a hypothetical Earth–Moon system. This allowed us to confidently apply it to the less well understood system Trappist-1, and show that the differences in TTVs could reach a few seconds for a four year measurements, and planetary interactions could push planets f, g and h out of the synchronized states, which are consistent with Bolmont et al. (2020) and Vinson et al. (2019).

We assume the objects are rigid bodies in our simulation package. This is a good approximation when the deformation of the objects are slow. Thus, our simulation package can be applied for objects with a slow change of rotation rate or tidal distortion. When the deformation rate is faster than the orbital variation timescales, spin–orbit coupling using hydrodynamical simulations could provide more accurate results (e.g., Li et al. 2021). Beyond planetary systems, the rigid-body integrator can also be applied to asteroid binaries, which exhibit interesting dynamical properties due to spin-orbit coupling (Fahnestock & Scheeres 2008; Davis & Scheeres 2020; Meyer & Scheeres 2021).

The authors thank Sergio Blanes, Matija Ćuk, David Michael Hernandez, and Billy Quarles for helpful discussions. We also thank the anonymous review which significantly improved the quality of this article. R.C. and M.T. are grateful for the partial support by NSF DMS-1847802. G.L. is grateful for the partial support by NASA 80NNSC20K0641 and 80NNSC20K0522.

Appendix A Approximation of the Potential Energy

The procedure to approximate $V(\mathbf{q}_i, \mathbf{q}_j, \mathbf{R}_i, \mathbf{R}_j)$ in Equation (9) by Taylor expansion is shown below:

$$\begin{aligned}
 V(\mathbf{q}_i, \mathbf{q}_j, \mathbf{R}_i, \mathbf{R}_j) &= \int_{\mathcal{B}_i} \int_{\mathcal{B}_j} \frac{\mathcal{G}\rho(\mathbf{x}_i)\rho(\mathbf{x}_j)}{\|(\mathbf{q}_i + \mathbf{R}_i\mathbf{x}_i) - (\mathbf{q}_j + \mathbf{R}_j\mathbf{x}_j)\|} d\mathbf{x}_i d\mathbf{x}_j = \int_{\mathcal{B}_i} \int_{\mathcal{B}_j} \\
 &- \frac{\mathcal{G}\rho(\mathbf{x}_i)\rho(\mathbf{x}_j)}{\sqrt{\|\mathbf{q}_i - \mathbf{q}_j\|^2 + \|\mathbf{R}_i\mathbf{x}_i - \mathbf{R}_j\mathbf{x}_j\|^2 + 2(\mathbf{q}_i - \mathbf{q}_j)^T(\mathbf{R}_i\mathbf{x}_i - \mathbf{R}_j\mathbf{x}_j)}} \times d\mathbf{x}_i d\mathbf{x}_j = \int_{\mathcal{B}_i} \int_{\mathcal{B}_j} -\frac{\mathcal{G}\rho(\mathbf{x}_i)\rho(\mathbf{x}_j)}{\|\mathbf{q}_i - \mathbf{q}_j\|} \\
 &\times \left(1 - \frac{1}{2} \left[\frac{\|\mathbf{R}_i\mathbf{x}_i - \mathbf{R}_j\mathbf{x}_j\|^2 + 2(\mathbf{q}_i - \mathbf{q}_j)^T(\mathbf{R}_i\mathbf{x}_i - \mathbf{R}_j\mathbf{x}_j)}{\|\mathbf{q}_i - \mathbf{q}_j\|^2} \right] \right. \\
 &\left. + \frac{3}{8} \left[\frac{\|\mathbf{R}_i\mathbf{x}_i - \mathbf{R}_j\mathbf{x}_j\|^2 + 2(\mathbf{q}_i - \mathbf{q}_j)^T(\mathbf{R}_i\mathbf{x}_i - \mathbf{R}_j\mathbf{x}_j)}{\|\mathbf{q}_i - \mathbf{q}_j\|^2} \right]^2 \right) \\
 &\times d\mathbf{x}_i d\mathbf{x}_j + \mathcal{O}(\eta^3) = -\frac{\mathcal{G}m_i m_j}{\|\mathbf{q}_i - \mathbf{q}_j\|} + \frac{\mathcal{G}(m_i \text{Tr}[\mathbf{J}_i^{(d)}] + m_j \text{Tr}[\mathbf{J}_j^{(d)}])}{2 \|\mathbf{q}_i - \mathbf{q}_j\|^3} \\
 &- \frac{3\mathcal{G}(\mathbf{q}_i - \mathbf{q}_j)^T(m_j \mathbf{R}_i \mathbf{J}_i^{(d)} \mathbf{R}_i^T + m_i \mathbf{R}_j \mathbf{J}_j^{(d)} \mathbf{R}_j^T)(\mathbf{q}_i - \mathbf{q}_j)}{2 \|\mathbf{q}_i - \mathbf{q}_j\|^5} + \mathcal{O}(\eta^3) \quad (\text{A1})
 \end{aligned}$$

where $\eta = \frac{\max(\mathcal{R}_i, \mathcal{R}_j)}{\|\mathbf{q}_i - \mathbf{q}_j\|}$ (\mathcal{R}_i is the largest distance from the center in the i th body). If we use \mathbf{J} instead of \mathbf{J}_d , we have

$$\begin{aligned}
 V(\mathbf{q}_i, \mathbf{q}_j, \mathbf{R}_i, \mathbf{R}_j) &= -\frac{\mathcal{G}m_i m_j}{\|\mathbf{q}_i - \mathbf{q}_j\|} - \frac{\mathcal{G}(m_i \text{Tr}[\mathbf{J}_i] + m_j \text{Tr}[\mathbf{J}_j])}{2 \|\mathbf{q}_i - \mathbf{q}_j\|^3} \\
 &+ \frac{3\mathcal{G}(\mathbf{q}_i - \mathbf{q}_j)^T(m_j \mathbf{R}_i \mathbf{J}_i \mathbf{R}_i^T + m_i \mathbf{R}_j \mathbf{J}_j \mathbf{R}_j^T)(\mathbf{q}_i - \mathbf{q}_j)}{2 \|\mathbf{q}_i - \mathbf{q}_j\|^5} \\
 &+ \mathcal{O}(\eta^3) \quad (\text{A2})
 \end{aligned}$$

Higher order expansions:

$$\begin{aligned}
 V(\mathbf{q}_i, \mathbf{q}_j, \mathbf{R}_i, \mathbf{R}_j) &= \mathcal{G}m_i m_j \left\{ -\frac{1}{\|\mathbf{q}_i - \mathbf{q}_j\|} + \frac{1}{2 \|\mathbf{q}_i - \mathbf{q}_j\|^3} \right. \\
 &\times \left[\frac{1}{5} (a_i^2 + b_i^2 + c_i^2 + a_j^2 + b_j^2 + c_j^2) \right] - \frac{3}{2 \|\mathbf{q}_i - \mathbf{q}_j\|^5} (\mathbf{q}_i - \mathbf{q}_j)^T \\
 &\times \left(\mathbf{R}_i \frac{1}{5} \begin{bmatrix} a_i^2 & 0 & 0 \\ 0 & b_i^2 & 0 \\ 0 & 0 & c_i^2 \end{bmatrix} \mathbf{R}_i^T + \mathbf{R}_j \frac{1}{5} \begin{bmatrix} a_j^2 & 0 & 0 \\ 0 & b_j^2 & 0 \\ 0 & 0 & c_j^2 \end{bmatrix} \mathbf{R}_j^T \right) (\mathbf{q}_i - \mathbf{q}_j) \\
 &- \frac{3}{8 \|\mathbf{q}_i - \mathbf{q}_j\|^5} \left(\frac{1}{35} (3a_i^4 + 3b_i^4 + 3c_i^4 + 2(a_i^2 b_i^2 + a_i^2 c_i^2 + b_i^2 c_i^2)) \right. \\
 &+ \left. \frac{1}{35} (3a_j^4 + 3b_j^4 + 3c_j^4 + 2(a_j^2 b_j^2 + a_j^2 c_j^2 + b_j^2 c_j^2)) \right) \\
 &- \frac{3}{4 \|\mathbf{q}_i - \mathbf{q}_j\|^5} \text{Tr} \left[\mathbf{R}_i^T \mathbf{R}_j \frac{1}{5} \begin{bmatrix} a_j^2 & 0 & 0 \\ 0 & b_j^2 & 0 \\ 0 & 0 & c_j^2 \end{bmatrix} \mathbf{R}_j^T \right. \\
 &\times \left. \mathbf{R}_i \frac{1}{5} \begin{bmatrix} a_i^2 & 0 & 0 \\ 0 & b_i^2 & 0 \\ 0 & 0 & c_i^2 \end{bmatrix} \right] + \frac{15}{4 \|\mathbf{q}_i - \mathbf{q}_j\|^7} \left((\mathbf{q}_i - \mathbf{q}_j)^T \mathbf{R}_i \frac{1}{35} \right. \\
 &\times \left. \begin{bmatrix} a_i^2 (3a_i^3 + b_i^2 + c_i^2) & 0 & 0 \\ 0 & b_i^2 (a_i^2 + 3b_i^2 + c_i^2) & 0 \\ 0 & 0 & c_i^2 (a_i^2 + b_i^2 + 3c_i^2) \end{bmatrix} \right. \\
 &\times \left. \mathbf{R}_i^T (\mathbf{q}_i - \mathbf{q}_j) \right) + \frac{15}{4 \|\mathbf{q}_i - \mathbf{q}_j\|^7} \left((\mathbf{q}_i - \mathbf{q}_j)^T \mathbf{R}_j \frac{1}{35} \right. \\
 &\times \left. \begin{bmatrix} a_j^2 (3a_j^3 + b_j^2 + c_j^2) & 0 & 0 \\ 0 & b_j^2 (a_j^2 + 3b_j^2 + c_j^2) & 0 \\ 0 & 0 & c_j^2 (a_j^2 + b_j^2 + 3c_j^2) \end{bmatrix} \right. \\
 &\times \left. \mathbf{R}_j^T (\mathbf{q}_i - \mathbf{q}_j) \right) + \frac{15}{4 \|\mathbf{q}_i - \mathbf{q}_j\|^7} \left(\frac{1}{5} (a_i^2 + b_i^2 + c_i^2) \right. \\
 &\times \left. (\mathbf{q}_i - \mathbf{q}_j)^T \mathbf{R}_i \frac{1}{5} \begin{bmatrix} a_j^2 & 0 & 0 \\ 0 & b_j^2 & 0 \\ 0 & 0 & c_j^2 \end{bmatrix} \mathbf{R}_j^T (\mathbf{q}_i - \mathbf{q}_j) \right) \\
 &+ \frac{15}{4 \|\mathbf{q}_i - \mathbf{q}_j\|^7} \left(\frac{1}{5} (a_j^2 + b_j^2 + c_j^2) (\mathbf{q}_i - \mathbf{q}_j)^T \mathbf{R}_i \frac{1}{5} \right. \\
 &\times \left. \begin{bmatrix} a_i^2 & 0 & 0 \\ 0 & b_i^2 & 0 \\ 0 & 0 & c_i^2 \end{bmatrix} \mathbf{R}_i^T (\mathbf{q}_i - \mathbf{q}_j) \right) + \frac{15}{\|\mathbf{q}_i - \mathbf{q}_j\|^7} ((\mathbf{q}_i - \mathbf{q}_j)^T
 \end{aligned}$$

$$\begin{aligned}
& \times \mathbf{R}_i \frac{1}{5} \begin{bmatrix} a_i^2 & 0 & 0 \\ 0 & b_i^2 & 0 \\ 0 & 0 & c_i^2 \end{bmatrix} \mathbf{R}_i^T \mathbf{R}_j \frac{1}{5} \begin{bmatrix} a_j^2 & 0 & 0 \\ 0 & b_j^2 & 0 \\ 0 & 0 & c_j^2 \end{bmatrix} \mathbf{R}_j^T (\mathbf{q}_i - \mathbf{q}_j) \Big) \\
& - \frac{35}{8 \|\mathbf{q}_i - \mathbf{q}_j\|^9} \left(\text{Tr} \left[(\mathbf{q}_i - \mathbf{q}_j)(\mathbf{q}_i - \mathbf{q}_j)^T \mathbf{R}_i \frac{3}{35} \right. \right. \\
& \times \left. \begin{bmatrix} a_i^4 & 0 & 0 \\ 0 & b_i^4 & 0 \\ 0 & 0 & c_i^4 \end{bmatrix} \mathbf{R}_i^T (\mathbf{q}_i - \mathbf{q}_j)(\mathbf{q}_i - \mathbf{q}_j)^T \right] \right) \\
& - \frac{35}{8 \|\mathbf{q}_i - \mathbf{q}_j\|^9} \left(\text{Tr} \left[(\mathbf{q}_i - \mathbf{q}_j)(\mathbf{q}_i - \mathbf{q}_j)^T \mathbf{R}_j \frac{3}{35} \right. \right. \\
& \times \left. \begin{bmatrix} a_j^4 & 0 & 0 \\ 0 & b_j^4 & 0 \\ 0 & 0 & c_j^4 \end{bmatrix} \mathbf{R}_j^T (\mathbf{q}_i - \mathbf{q}_j)(\mathbf{q}_i - \mathbf{q}_j)^T \right] \right) \\
& - \frac{105}{4 \|\mathbf{q}_i - \mathbf{q}_j\|^9} (\mathbf{q}_i - \mathbf{q}_j)^T \mathbf{R}_i \frac{1}{5} \begin{bmatrix} a_i^2 & 0 & 0 \\ 0 & b_i^2 & 0 \\ 0 & 0 & c_i^2 \end{bmatrix} \\
& \times \mathbf{R}_i^T (\mathbf{q}_i - \mathbf{q}_j)(\mathbf{q}_i - \mathbf{q}_j)^T \mathbf{R}_j \frac{1}{5} \begin{bmatrix} a_j^2 & 0 & 0 \\ 0 & b_j^2 & 0 \\ 0 & 0 & c_j^2 \end{bmatrix} \\
& \times \mathbf{R}_j^T (\mathbf{q}_i - \mathbf{q}_j) \} + \mathcal{O}(\eta^5). \tag{A3}
\end{aligned}$$

A.1. Properties of the hat-map

With $\mathbf{u}, \mathbf{v}, \mathbf{w} \in \mathbb{R}^3$, $\mathbf{D} = \begin{bmatrix} d_1 & 0 & 0 \\ 0 & d_2 & 0 \\ 0 & 0 & d_3 \end{bmatrix}$, we have

1. $\hat{\mathbf{u}}\hat{\mathbf{v}} = \mathbf{u} \times \mathbf{v}$.
2. $\hat{\mathbf{u}} \times \hat{\mathbf{v}} = \hat{\mathbf{u}}\hat{\mathbf{v}} - \hat{\mathbf{v}}\hat{\mathbf{u}}$.
3. $\hat{\mathbf{u}}\mathbf{D} - \mathbf{D}\hat{\mathbf{u}}^T = \text{Tr}[\mathbf{D}]\hat{\mathbf{u}} - \widehat{\mathbf{D}\mathbf{u}}$.
4. $\hat{\mathbf{u}}^T\hat{\mathbf{u}}\mathbf{D} - \mathbf{D}\hat{\mathbf{u}}^T\hat{\mathbf{u}} = \mathbf{u} \times \widehat{\mathbf{D}\mathbf{u}}$.

Appendix B

Review: Equations of Motion of One Rigid Body in an External Potential

We will review two equivalent approaches.

B.1. Approach 1: Derivation from a Constrained Hamiltonian System

We can view \mathbf{R} to be in the embedded Euclidean space $\mathbb{R}^{3 \times 3} \leftrightarrow \text{SO}(3)$ and use $\mathbf{R} \in \text{SO}(3)$ as a holonomic constraint. The Lagrangian L (Equation (11)) has 9-DOF before applying the constraint $\mathbf{R} \in \text{SO}(3)$. The conjugate variable of $\mathbf{R}(t)$ will be denoted by $\mathbf{P}(t)$.

The constraint of a system forces the evolution of the system in a specific manifold, and the manifold can be directly calculated from the constraint (one may refer Chapter VII of

Hairer et al. (2006) for details). For rigid-body dynamics represented by a rotation matrix $\mathbf{R}(t)$, the constraint is $\mathbf{R}(t)^T \mathbf{R}(t) - \mathbf{I}_{3 \times 3} = \mathbf{0}_{3 \times 3}$. Reich & Zentrum (1996) and Hairer et al. (2006) have shown the procedure of finding equations of motion by utilizing the constraint for a rigid-body system with a \mathbf{R} dependent potential. By using Lagrange multipliers (Hairer et al. 2006) for the constraint $\mathbf{R}^T \mathbf{R} - \mathbf{I}_{3 \times 3} = \mathbf{0}$, we have the following Lagrangian,

$$\begin{aligned}
L(\mathbf{R}, \dot{\mathbf{R}}) &= \frac{1}{2} \text{Tr}[\dot{\mathbf{R}} \mathbf{J}_d \dot{\mathbf{R}}^T] - V(\mathbf{R}) \\
& - \frac{1}{2} \text{Tr}(\mathbf{\Lambda}^T (\mathbf{R}^T \mathbf{R} - \mathbf{I}_{3 \times 3})), \tag{B1}
\end{aligned}$$

with 6-dim Lagrange multipliers $\mathbf{\Lambda} = \begin{bmatrix} \lambda_1 & \lambda_4 & \lambda_6 \\ \lambda_4 & \lambda_2 & \lambda_5 \\ \lambda_6 & \lambda_5 & \lambda_3 \end{bmatrix} \in \mathbb{R}^{3 \times 3}$ a symmetric matrix.

Doing Legendre transform for Equation (B1), we have

$$\mathbf{P} = \frac{\partial L(\mathbf{R}, \dot{\mathbf{R}})}{\partial \dot{\mathbf{R}}} = \dot{\mathbf{R}} \mathbf{J}_d, \tag{B2}$$

and the corresponding Hamiltonian,

$$\begin{aligned}
H(\mathbf{R}, \mathbf{P}) &= \frac{1}{2} \text{Tr}[\mathbf{P} \mathbf{J}_d^{-1} \mathbf{P}^T] + V(\mathbf{R}) \\
& + \frac{1}{2} \text{Tr}(\mathbf{\Lambda}^T (\mathbf{R}^T \mathbf{R} - \mathbf{I}_{3 \times 3})). \tag{B3}
\end{aligned}$$

As the constraint for \mathbf{R} is $\mathbf{R}^T \mathbf{R} = \mathbf{I}_{3 \times 3}$, according to Hairer et al. (2006), the constraint for \mathbf{P} can be obtained by taking time derivative for $\mathbf{R}^T \mathbf{R} - \mathbf{I}_{3 \times 3} = \mathbf{0}_{3 \times 3}$, i.e., $\mathbf{J}_d^{-1} \mathbf{P}^T \mathbf{R} + \mathbf{R}^T \mathbf{P} \mathbf{J}_d^{-1} = \mathbf{0}_{3 \times 3}$.

So,

$$\begin{cases} \dot{\mathbf{R}} = \frac{\partial H}{\partial \mathbf{P}} = \mathbf{P} \mathbf{J}_d^{-1}, \\ \dot{\mathbf{P}} = -\frac{\partial H}{\partial \mathbf{R}} = -\frac{\partial V(\mathbf{R})}{\partial \mathbf{R}} - \mathbf{R} \mathbf{\Lambda}, \end{cases} \tag{B4}$$

on the manifold

$$\mathcal{M} = \{(\mathbf{R}, \mathbf{P}) | \mathbf{R}^T \mathbf{R} = \mathbf{I}_{3 \times 3}, \mathbf{J}_d^{-1} \mathbf{P}^T \mathbf{R} + \mathbf{R}^T \mathbf{P} \mathbf{J}_d^{-1} = \mathbf{0}_{3 \times 3}\}. \tag{B5}$$

Note that $\hat{\mathbf{\Omega}} = \mathbf{R}^T \mathbf{P} \mathbf{J}_d^{-1}$ with $\mathbf{\Omega}$ being the body's angular velocity. Taking time derivative for $\hat{\mathbf{\Omega}}$, we have

$$\hat{\mathbf{\Omega}} = \mathbf{J}_d^{-1} \mathbf{P}^T \mathbf{P} \mathbf{J}_d^{-1} + \mathbf{R}^T \left(-\frac{\partial V(\mathbf{R})}{\partial \mathbf{R}} - \mathbf{R} \mathbf{\Lambda} \right) \mathbf{J}_d^{-1}. \tag{B6}$$

Physically, we want to find dynamics of \mathbf{R} and the body's angular momentum $\mathbf{\Pi}$. Since $\hat{\mathbf{\Pi}} = \widehat{\mathbf{\Omega}} = \text{Tr}[\mathbf{J}_d] \hat{\mathbf{\Omega}} - \widehat{\mathbf{J}_d \mathbf{\Omega}} = \hat{\mathbf{\Omega}} \mathbf{J}_d - \mathbf{J}_d \hat{\mathbf{\Omega}}^T$ (see Appendix A.1), we may find dynamics of $\mathbf{\Pi}$,

$$\begin{aligned}
\widehat{\mathbf{\Pi}} &= (\mathbf{J}_d^{-1} \mathbf{P}^T \mathbf{P} - \mathbf{P}^T \mathbf{P} \mathbf{J}_d^{-1}) \\
& + \left(\left(\frac{\partial V(\mathbf{R})}{\partial \mathbf{R}} \right)^T \mathbf{R} - \mathbf{R}^T \frac{\partial V(\mathbf{R})}{\partial \mathbf{R}} \right), \tag{B7}
\end{aligned}$$

with the symmetric $\mathbf{\Lambda}$ vanished.⁷

⁷ Since $\mathbf{\Lambda}$ is symmetric, applying $\hat{\mathbf{\Omega}} \in \mathfrak{so}(3)$, $\mathbf{\Lambda}$ can actually be solved from Equation (B6).

As $\mathbf{P} = \mathbf{R}\hat{\Omega}\mathbf{J}_d$, properties of hat-map (see Appendix A.1) lead to

$$\begin{aligned}\hat{\Pi} &= (\hat{\Omega}^T \hat{\Omega} \mathbf{J}_d - \mathbf{J}_d \hat{\Omega}^T \hat{\Omega}) + \left(\left(\frac{\partial V(\mathbf{R})}{\partial \mathbf{R}} \right)^T \mathbf{R} - \mathbf{R}^T \frac{\partial V(\mathbf{R})}{\partial \mathbf{R}} \right) \\ &= \widehat{\Omega \times J_d \Omega} + \left(\left(\frac{\partial V(\mathbf{R})}{\partial \mathbf{R}} \right)^T \mathbf{R} - \mathbf{R}^T \frac{\partial V(\mathbf{R})}{\partial \mathbf{R}} \right).\end{aligned}\quad (\text{B8})$$

Thus

$$\begin{aligned}\hat{\Pi} &= \Omega \times J_d \Omega - \left(\mathbf{R}^T \frac{\partial V(\mathbf{R})}{\partial \mathbf{R}} - \left(\frac{\partial V(\mathbf{R})}{\partial \mathbf{R}} \right)^T \mathbf{R} \right)^\vee \\ &= \Omega \times (Tr[\mathbf{J}_d] - \mathbf{J}) \Omega - \left(\mathbf{R}^T \frac{\partial V(\mathbf{R})}{\partial \mathbf{R}} - \left(\frac{\partial V(\mathbf{R})}{\partial \mathbf{R}} \right)^T \mathbf{R} \right)^\vee \\ &= -\Omega \times \mathbf{J} \Omega - \left(\mathbf{R}^T \frac{\partial V(\mathbf{R})}{\partial \mathbf{R}} - \left(\frac{\partial V(\mathbf{R})}{\partial \mathbf{R}} \right)^T \mathbf{R} \right)^\vee \\ &= \Pi \times \mathbf{J}^{-1} \Pi - \left(\mathbf{R}^T \frac{\partial V(\mathbf{R})}{\partial \mathbf{R}} - \left(\frac{\partial V(\mathbf{R})}{\partial \mathbf{R}} \right)^T \mathbf{R} \right)^\vee\end{aligned}\quad (\text{B9})$$

So, the equations of motion with respect to \mathbf{R} and Π for a one rigid-body system are

$$\begin{cases} \dot{\mathbf{R}} = \widehat{\mathbf{R} J^{-1} \Pi}, \\ \dot{\Pi} = \Pi \times \mathbf{J}^{-1} \Pi - \left(\mathbf{R}^T \frac{\partial V(\mathbf{R})}{\partial \mathbf{R}} - \left(\frac{\partial V(\mathbf{R})}{\partial \mathbf{R}} \right)^T \mathbf{R} \right)^\vee. \end{cases} \quad (\text{B10})$$

B.2. Approach 2: Variational Principle for Mechanics on a Lie Group

Obtaining a Euler–Lagrange equation for the Hamilton’s variational principle on a Lie group has been well studied (e.g., Marsden & Ratiu 1994; Holm et al. 2009). Here, we summarize the results for the special case of rigid bodies from the expository part of Lee et al. (2005).

Denote the infinitesimally varied rotation by $\mathbf{R}_\epsilon = \mathbf{R} \exp(\epsilon \hat{\eta})$ with $\epsilon \in \mathbb{R}$ and $\eta \in \mathbb{R}^3$, where $\exp(\cdot)$ is a mapping from $\mathfrak{so}(3)$ to $\text{SO}(3)$. The varied angular velocity is

$$\begin{aligned}\hat{\Omega}_\epsilon &= \mathbf{R}_\epsilon^T \dot{\mathbf{R}}_\epsilon = e^{-\epsilon \hat{\eta}} \mathbf{R}^T (\dot{\mathbf{R}} e^{\epsilon \hat{\eta}} + \mathbf{R} \cdot e^{\epsilon \hat{\eta}} \epsilon \hat{\eta}) \\ &= e^{-\epsilon \hat{\eta}} \hat{\Omega} e^{\epsilon \hat{\eta}} + \epsilon \hat{\eta} \\ &= \hat{\Omega} + \epsilon \{ \hat{\eta} + \hat{\Omega} \hat{\eta} - \hat{\eta} \hat{\Omega} \} + \mathcal{O}(\epsilon^2).\end{aligned}\quad (\text{B11})$$

Consider the action

$$\begin{aligned}S(\Omega, \mathbf{R}) &= \int_{t_0}^{t_1} L(\Omega, \mathbf{R}) dt \\ &= \int_{t_0}^{t_1} \frac{1}{2} \text{Tr}[\hat{\Omega} \mathbf{J}_d \hat{\Omega}^T] - V(\mathbf{R}) dt.\end{aligned}\quad (\text{B12})$$

Taking the variation of the action S , we have

$$\begin{aligned}S_\epsilon(\Omega, \mathbf{R}) &= S(\Omega_\epsilon, \mathbf{R}_\epsilon) \\ &= S(\Omega, \mathbf{R}) + \epsilon \int_{t_0}^{t_1} \frac{1}{2} \text{Tr}[-\hat{\eta}(\mathbf{J}_d \hat{\Omega} + \hat{\Omega} \mathbf{J}_d) \\ &\quad + \hat{\eta} \hat{\Omega}(\mathbf{J}_d \hat{\Omega} + \hat{\Omega} \mathbf{J}_d) - \hat{\eta}(\mathbf{J}_d \hat{\Omega} + \hat{\Omega} \mathbf{J}_d \hat{\Omega})] \\ &\quad + \text{Tr} \left[\hat{\eta} \mathbf{R}^T \frac{\partial \mathbf{R}}{\partial \mathbf{R}} \right] dt + \mathcal{O}(\epsilon^2).\end{aligned}\quad (\text{B13})$$

Using *Hamilton’s Principle*, we have $\frac{d}{d\epsilon} \Big|_{\epsilon=0} S_\epsilon = 0$, i.e.

$$\frac{1}{2} \int_{t_0}^{t_1} \text{Tr} \left[\hat{\eta} \left\{ \widehat{\mathbf{J} \dot{\Omega}} + \widehat{\Omega \times J \Omega} + 2 \mathbf{R}^T \frac{\partial V}{\partial \mathbf{R}} \right\} \right] = 0 \quad (\text{B14})$$

for any $\eta \in \mathbb{R}^3$. Therefore, $\left\{ \widehat{\mathbf{J} \dot{\Omega}} + \widehat{\Omega \times J \Omega} + 2 \mathbf{R}^T \frac{\partial V}{\partial \mathbf{R}} \right\}$ must be skew-symmetric, which gives us

$$\widehat{\mathbf{J} \dot{\Omega}} = -\widehat{\Omega \times J \Omega} + \left(\frac{\partial V^T}{\partial \mathbf{R}} \mathbf{R} - \mathbf{R}^T \frac{\partial V}{\partial \mathbf{R}} \right). \quad (\text{B15})$$

Thus

$$\widehat{\Pi} = \widehat{\Pi \times J^{-1} \Pi} + \left(\frac{\partial V^T}{\partial \mathbf{R}} \mathbf{R} - \mathbf{R}^T \frac{\partial V}{\partial \mathbf{R}} \right). \quad (\text{B16})$$

Appendix C Proof of the Hierarchical Composition Error

Theorem 1. Given four Hamiltonian flows $\{\varphi_t^{[i]}\}_{i=1}^4$ of \mathbf{H}_i with $\mathbf{H} = \mathbf{H}_1 + \mathbf{H}_2 + \mathbf{H}_3 + \mathbf{H}_4$. Construct an integrator $\varphi_h := \mathcal{C}_3(\mathcal{C}_1(\varphi_h^{[1]}, \varphi_h^{[2]}), \mathcal{C}_2(\varphi_h^{[3]}, \varphi_h^{[4]}))$ via composition methods \mathcal{C}_i , $i = 1, 2, 3$ such that

$$\begin{aligned}\mathcal{C}_i(\varphi_h^A, \varphi_h^B) &= \varphi_{a_1^{[i]} h}^A \circ \varphi_{b_1^{[i]} h}^B \circ \varphi_{a_2^{[i]} h}^A \circ \varphi_{b_2^{[i]} h}^B \\ &\quad \circ \cdots \varphi_{a_{n_i}^{[i]} h}^A \circ \varphi_{b_{n_i}^{[i]} h}^B.\end{aligned}$$

Then, $\mathcal{E}(\varphi_h)$ equals to the summation of orders of \mathcal{C}_i , $i = 1, 2, 3$ with $\mathcal{E}(\cdot)$ being the global error function.

Proof. Assume that the associated Lie operators of $\varphi_t^{[i]}$ ’s vector fields are \mathcal{L}_{H_i} . There exists a Lie operator A_1 such that for $\mathcal{C}_1(\varphi_h^{[1]}, \varphi_h^{[2]})$,

$$\begin{aligned}e^{a_1^{[1]} \mathcal{L}_{H_1}} e^{b_1^{[1]} \mathcal{L}_{H_2}} e^{a_2^{[1]} \mathcal{L}_{H_1}} e^{b_2^{[1]} \mathcal{L}_{H_2}} \cdots e^{a_{n_1}^{[1]} \mathcal{L}_{H_1}} \\ \times e^{b_{n_1}^{[1]} \mathcal{L}_{H_2}} = e^{A_1} = e^{\mathcal{L}_{H_1} + \mathcal{L}_{H_2} + E_1}\end{aligned}$$

with the order of E_1 equals the order of \mathcal{C}_1 . Similarly, we have

$$\begin{aligned}e^{a_1^{[2]} \mathcal{L}_{H_3}} e^{b_1^{[2]} \mathcal{L}_{H_4}} e^{a_2^{[2]} \mathcal{L}_{H_3}} e^{b_2^{[2]} \mathcal{L}_{H_4}} \cdots e^{a_{n_2}^{[2]} \mathcal{L}_{H_3}} \\ \times e^{b_{n_2}^{[2]} \mathcal{L}_{H_4}} = e^{A_2} = e^{\mathcal{L}_{H_3} + \mathcal{L}_{H_4} + E_2}\end{aligned}$$

with the order of E_2 equals the order of \mathcal{C}_2 . Further for \mathcal{C}_3 ,

$$\begin{aligned}e^{a_1^{[3]} A_1} e^{b_1^{[3]} A_2} e^{a_2^{[3]} A_1} e^{b_2^{[3]} A_2} \cdots e^{a_{n_3}^{[3]} A_1} e^{b_{n_3}^{[3]} A_2} \\ = e^{A_3} = e^{A_1 + A_2 + E_3} = e^{\mathcal{L}_{H_1} + \mathcal{L}_{H_2} + \mathcal{L}_{H_3} + \mathcal{L}_{H_4} + E_1 + E_2 + E_3},\end{aligned}$$

with the order of E_3 equals the order of \mathcal{C}_3 . Therefore, the global error of φ_h is the summation of the orders of \mathcal{C}_i , $i = 1, 2, 3$. \square

Appendix D Composition Methods

Symplectic integrators of a Hamiltonian system $H = A + B$ can be constructed by composing the flows of A and B . We list the composition methods used in the paper below for the general $H = A + B$ and perturbative Hamiltonian $H = A + \varepsilon B$ in Tables 5 and 6, respectively.

Table 5

Composition Methods $\mathcal{C}(\cdot, \cdot)$ of General $H = A + B$. φ_h^A and φ_h^B are Flows of A and B , Respectively

Composition Method	Order
$\mathcal{C}_{\text{Euler}}(\varphi_h^A, \varphi_h^B) := \varphi_h^A \circ \varphi_h^B$	(1)
$\mathcal{C}_{\text{Verlet}}(\varphi_h^A, \varphi_h^B) := \varphi_{h/2}^A \circ \varphi_h^B \circ \varphi_{h/2}^A$	(2)
$\mathcal{C}_{\text{TriJump}}(\varphi_h^A, \varphi_h^B) := \varphi_{\gamma_1 h} \circ \varphi_{\gamma_2 h} \circ \varphi_{\gamma_1 h}$	(4)
with $\varphi_h := \mathcal{C}_{\text{Verlet}}(\varphi_h^A, \varphi_h^B)$ and $\gamma_1 = 1/(2 - 2^{1/3})$, $\gamma_2 = 1 - 2\gamma_1$ (Suzuki 1990).	
$\mathcal{C}_{S6}(\varphi_h^A, \varphi_h^B) := \varphi_{a_1 h} \circ \varphi_{a_2 h} \circ \varphi_{a_3 h} \circ \varphi_{a_4 h} \circ \varphi_{a_3 h} \circ \varphi_{a_2 h} \circ \varphi_{a_1 h}$	(6)
with $\varphi_h := \mathcal{C}_{\text{Verlet}}(\varphi_h^A, \varphi_h^B)$ and $a_1 = 0.784513610477560$, $a_2 = 0.235573213359357$, $a_3 = -1.17767998417887$, $a_4 = 1 - 2(a_1 + a_2 + a_3)$ (Yoshida 1990)	

Table 6

Composition Methods $\mathcal{C}(\cdot, \cdot)$ of Perturbative $H = A + \varepsilon B$. φ_h^A and φ_h^B are Flows of A and εB , Respectively

Composition method	Order
$\mathcal{C}_{BAB22}(\varphi_h^A, \varphi_h^B) = \varphi_{h/2}^B \circ \varphi_h^A \circ \varphi_{h/2}^B$	(-, 2, 2)
$\mathcal{C}_{ABA22}(\varphi_h^A, \varphi_h^B) = \varphi_{h/2}^A \circ \varphi_h^B \circ \varphi_{h/2}^A$	(-, 2, 2)
$\mathcal{C}_{ABA42}(\varphi_h^A, \varphi_h^B) = \varphi_{\frac{(3-\sqrt{3})h}{6}}^A \circ \varphi_{\frac{h}{2}}^B \circ \varphi_{\frac{h}{\sqrt{3}}}^A \circ \varphi_{\frac{h}{2}}^B \circ \varphi_{\frac{(3-\sqrt{3})h}{6}}^A$ (\mathcal{SABA}_2 in (Laskar & Robutel 2001) or equivalently the order (4, 2) ABA method with $s = 2$ in (McLachlan 1995))	(-, 4, 2)

ORCID iDs

Gongjie Li  <https://orcid.org/0000-0001-8308-0808>

References

Agol, E., Dorn, C., Grimm, S. L., et al. 2020, arXiv:2010.01074

Agol, E., & Fabrycky, D. C. 2018, in *Handbook of Exoplanets*, ed. H. J. Deeg & J. A. Belmonte (Cham: Springer), 797

Agol, E., Hernandez, D. M., & Langford, Z. 2021, *MNRAS*, 507, 1582

Anderson, J. D., Esposito, P. B., Martin, W., Thornton, C. L., & Muhleman, D. O. 1975, *ApJ*, 200, 221

Benitez, F., & Gallardo, T. 2008, *CeMDA*, 101, 289

Blanchet, L. 2006, *LRR*, 9, 4

Blanco-Cuaresma, S., & Bolmont, E. 2017, EWASS Special Session 4 (2017): Star-planet Interactions (EWASS-SS4-2017), arXiv:1712.01281

Blanes, S., & Casas, F. 2017, *A Concise Introduction to Geometric Numerical Integration* (Boca Raton, FL: CRC Press)

Blanes, S., Casas, F., Farres, A., Laskar, J., Makazaga, J., & Murua, A. 2013, *ApNM*, 68, 58

Blanes, S., Casas, F., & Murua, A. 2008, arXiv:0812.0377

Bolmont, E., Demory, B. O., Blanco-Cuaresma, S., et al. 2020, *A&A*, 635, A117

Bolmont, E., Raymond, S. N., Leconte, J., Hersant, F., & Correia, A. C. M. 2015, *A&A*, 583, A116

Bou-Rabee, N., & Marsden, J. E. 2009, *Foundations of Computational Mathematics*, 9, 197

Breiter, S., Nesvorný, D., & Vokrouhlický, D. 2005, *AJ*, 130, 1267

Celledoni, E., Fassò, F., Säfström, N., & Zanna, A. 2008, *SIAM Journal on Scientific Computing*, 30, 2084

Celledoni, E., Marthinsen, H., & Owren, B. 2014, *JCoPh*, 257, 1040

Chambers, J. E. 1999, *MNRAS*, 304, 793

Davis, A. B., & Scheeres, D. J. 2020, *PSJ*, 1, 25

Dullweber, A., Leimkuhler, B., & McLachlan, R. 1997, *JChPh*, 107, 5840

Duncan, M. J., Levison, H. F., & Lee, M. H. 1998, *AJ*, 116, 2067

Eggleton, P. P., Kiseleva, L. G., & Hut, P. 1998, *ApJ*, 499, 853

Eggleton, P. P., & Kiseleva-Eggleton, L. 2001, *ApJ*, 562, 1012

Fabrycky, D., & Tremaine, S. 2007, *ApJ*, 669, 1298

Fahnestock, E. G., & Scheeres, D. J. 2008, *Icarus*, 194, 410

Fassò, F. 2003, *JCoPh*, 189, 527

Giorgini, J., et al. 1996, *AAS/Division for Planetary Sciences Meeting Abstracts*, 28, 25–04

Grimm, S. L., Demory, B., Gillon, M., et al. 2018, *A&A*, 613, A68

Hairer, E., Lubich, C., & Wanner, G. 2006, *Geometric Numerical Integration: Structure-Preserving Algorithms for Ordinary Differential Equations* (2nd edn; Berlin: Springer)

Heyl, J. S., & Gladman, B. J. 2007, *MNRAS*, 377, 1511

Holm, D., Schmah, T., & Stoica, C. 2009, *Geometric Mechanics and Symmetry: From Finite to Infinite Dimensions*, Oxford Texts in Applied and Engineering Mathematics (Oxford: Oxford Univ. Press)

Hou, X., Scheeres, D. J., & Xin, X. 2017, *CeMDA*, 127, 369

Hut, P. 1981, *A&A*, 99, 126

Iserles, A., Munthe-Kaas, H. Z., Nørsett, S. P., & Zanna, A. 2000, *AcNum*, 9, 215

Joshi, M. M., Haberle, R. M., & Reynolds, R. T. 1997, *Icar*, 129, 450

Kasting, J. F., Whitmire, D. P., & Reynolds, R. T. 1993, *Icar*, 101, 108

Kreyche, S., Barnes, J., Quarles, B., & Chambers, J. *PSJ*, submitted

Laskar, J., Joutel, F., & Robutel, P. 1993, *Natur*, 361, 615

Laskar, J., & Robutel, P. 1993, *Natur*, 361, 608

Laskar, J., & Robutel, P. 2001, *CeMDA*, 80, 39

Lee, T., Leok, M., & McClamroch, N. H. 2007, *CeMDA*, 98, 121

Lee, T., McClamroch, N. H., & Leok, M. 2005, in *Proc. 2005 IEEE Conf. on Control Applications*, 2005 (CCA 2005., IEEE), 962

Leimkuhler, B., & Reich, S. 2004, *Cambridge Monographs on Applied and Computational Mathematics*, Vol. 14, *Simulating Hamiltonian Dynamics* (Cambridge: Cambridge Univ. Press), xvi+379

Li, G. 2021, *ApJL*, 915, L2

Li, G., & Batygin, K. 2014, *ApJ*, 790, 69

Li, J., Lai, D., Anderson, K. R., & Pu, B. 2021, *MNRAS*, 501, 1621

Lissauer, J. J., Barnes, J. W., & Chambers, J. E. 2012, *Icar*, 217, 77

Maciejewski, G., Fernández, M., Aceituno, F., et al. 2018, *AcA*, 68, 371

Mardling, R. A., & Lin, D. N. C. 2002, *ApJ*, 573, 829

Marsden, J. E., & Ratiu, T. S. 1994, *Introduction to Mechanics and Symmetry: A Basic Exposition of Classical Mechanical Systems* (Berlin: Springer)

McLachlan, R. I. 1995, *BIT Numerical Mathematics*, 35, 258

McLachlan, R. I., & Quispel, G. R. W. 2002, *AcNum*, 11, 341

Meyer, A. J., & Scheeres, D. J. 2021, *Icarus*, 367, 114554

Millholland, S., & Laughlin, G. 2019, *NatAs*, 3, 424

Miralda-Escudé, J. 2002, *ApJ*, 564, 1019

Muirhead, P. S., Mann, A. W., Vanderburg, A., et al. 2015, *ApJ*, 801, 18

Ragozzine, D., & Wolf, A. S. 2009, *ApJ*, 698, 1778

Reich, S., & Zentrum, K.-Z. 1996, *Fields Inst. Commun.*, 10, 181

Sanz-Serna, J., & Calvo, M. 1994, *Numerical Hamiltonian Problems* (1st edn; Berlin: Springer)

Suzuki, M. 1990, *PhL A*, 146, 319

Tamayo, D., Rein, H., Petrovich, C., & Murray, N. 2017, *ApJL*, 840, L19

Tamayo, D., Rein, H., Shi, P., & Hernandez, D. M. 2020, *MNRAS*, 491, 2885

Tao, M., & Ohsawa, T. 2020, in *Int. Conf. on Artificial Intelligence and Statistics (PMLR)*, 4269

Touma, J., & Wisdom, J. 1994, *AJ*, 107, 1189

Van Hoolst, T., Rambaux, N., Karatekin, Ö., Dehant, V., & Rivoldini, A. 2008, *Icar*, 195, 386

van Zon, R., & Schofield, J. 2007, *PhRvE*, 75, 056701

Vilmart, G. 2008, *JCoPh*, 227, 7083

Vinson, A. M., Tamayo, D., & Hansen, B. M. S. 2019, *MNRAS*, 488, 5739

Wisdom, J., & Holman, M. 1991, *AJ*, 102, 1528

Wordsworth, R. 2015, *ApJ*, 806, 180

Yoshida, H. 1990, *PhL A*, 150, 262

Zhu, W., Petrovich, C., Wu, Y., Dong, S., & Xie, J. 2018, *ApJ*, 860, 101